length of 175 μm at the indicated levels of injured spinal cords with a CCD camera (DXC-390; Sony, Tokyo, Japan) using a Micro Computer Imaging Device (MCID; Imaging Research Inc., St. Catharines, Ontario, Canada). The obtained images were analyzed using grain counting with the light intensity by MCID. Threshold values were maintained at constant levels for all analyses. Images of axial sections stained with hematoxylin and eosin were obtained, and manually outlined areas of cavitation were also quantified by MCID. Images of axial sections stained with anti-ChAT antibody and anti-RECA-1 antibody were obtained, and the numbers of ChAT-positive motoneurons in the ventral horns and the numbers of RECA-1-positive vessels with lumina larger than 20 μm were counted.

Behavioral Testing

Motor function of the hindlimbs was evaluated by open-field testing using the methodology of the Basso-Beattie-Bresnahan (BBB) scale at 4, 7, 14, 21, 28, 35, and 42 days after SCI (n = 14 for each group). Throughout the surgery, behavioral testing, and histological analyses, the three researchers who performed the procedures were unaware of the groups to which the rats belonged.

Statistical Analysis

All data are reported as the mean ± SEM. An unpaired two-tailed Student's t-test was used for single comparisons. The results of the real-time PCR and ELISA experiments were analyzed via Dunnett test. The Mann-Whitney U-test was used for the BBB score.

RESULTS

Endogenous Up-Regulation of HGF in Injured Spinal Cord Was Insufficient Compared With the Sharp Increase of c-Met Expression During the Acute Phase of SCI

To determine the dynamics of the HGF-c-Met system in adult rat spinal cord after SCI, the levels of HGF and c-Met mRNA expression in injured spinal cord were analyzed via real-time RT-PCR, and the amounts of HGF protein in injured spinal cord and plasma were also analyzed by an ELISA in the SCI group. Whereas the level of c-Met mRNA expression in injured spinal cord drastically increased from 1 day after SCI (Fig. 1A), the level of HGF mRNA expression gradually increased and peaked at 2 weeks after SCI (Fig. 1B). Thus HGF and c-Met mRNA expression peaked at different time points after SCI. Consistently with the level of HGF mRNA expression, the amount of HGF protein in injured spinal cord gradually increased, peaking at about 4 weeks after SCI (Fig. 1C). In contrast, the amount of HGF protein in the plasma did not increase after SCI (Fig. 1D). Next, we examined the localization of c-Met in normal and injured rat spinal cord. In intact thoracic spinal cord, c-Met immunoreactivity (c-Met-IR) was detected in NeuN-positive neurons and GST-π-positive oligodendrocytes, but not in astrocytes (Fig. 2A–I). However, at 1 week after SCI, c-Met-IR was clearly observed in GFAP-positive reactive astrocytes (Fig. 2J–L;
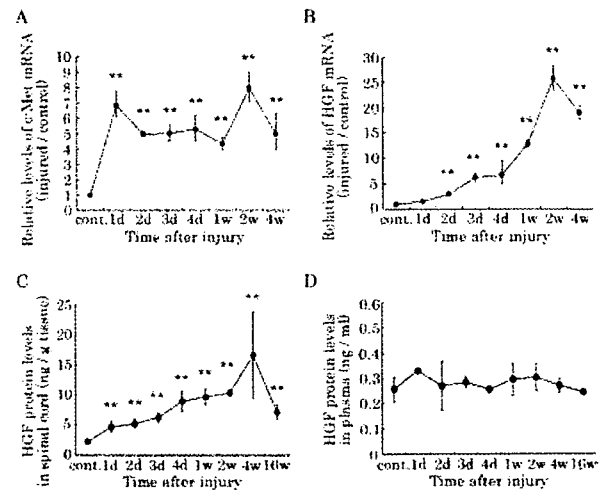

Fig. 1. Endogenous regulation of HGF and c-Met expression after SCI. The levels of c-Met mRNA and HGF mRNA expression after SCI in a 4-mm segment of spinal cord from the lesion epicenter were analyzed by using real-time RT-PCR. In contrast to a drastic increase in c-Met mRNA expression during the acute phase of SCI (A), HGF mRNA expression showed a gradual increase only during the subacute phase (B). ELISA data show that the amount of HGF protein in a 4-mm segment of spinal cord from the lesion epicenter gradually increased during the subacute phase of SCI (C), similar to the pattern of HGF mRNA expression, and the plasma HGF levels did not increase significantly after SCI (D). All data were reported as the mean ± SEM. **P < 0.01; n > 3 each.

axial section at 5 mm rostral to the epicenter) as well as in neurons and oligodendrocytes (data not shown).

To examine the distribution and amount of HGF protein in uninjured spinal cord after gene delivery, the spinal cord tissues were harvested and processed for an ELISA and HGF immunostaining at 3 days and 4 weeks after the HSV-1 vectors (HSV-HGF and HSV-LacZ) injection. Although HGF-IR showed a remarkable expansion putatively in the extracellular matrix in the HGF group at 3 days after injection, very little HGF-IR was observed in the LacZ group (Fig. 3A). Injection of the HSV-1 vectors resulted in a significantly higher amount of HGF protein in the HGF group (11.5 ± 0.8 ng/g tissue) compared with that in the LacZ group (3.4 ± 0.1 ng/g tissue) at 3 days after injection (Fig. 3C). Double immunostaining using anti-β-galactosidase antibody showed that LacZ gene expression was maintained in NeuN-positive neurons until 4 weeks after the injection (Fig. 3B). There was no significant difference in the amount of HGF protein between the HGF group (4.9 ± 1.5 ng/g tissue) and the LacZ group (2.9 ± 0.1 ng/g tissue) at 4 weeks after the injection (Fig. 3C).

HGF Promotes Survival of Neurons and Oligodendrocytes After SCI

To determine the effects of HGF gene delivery on the injured spinal cord, we performed several quantita-
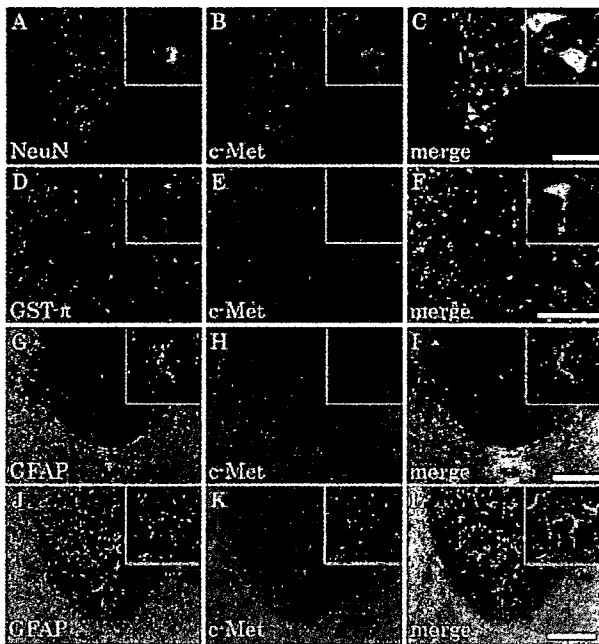
Fig. 2. Change in c-Met immunoreactivity (IR) in neurons, oligodendrocytes and astrocytes before and after SCI. Intact spinal cord showed c-Met-IR in NeuN-positive neurons (A–C) and GST-π-positive oligodendrocytes (D–F), but not in astrocytes (G–I). At 1 week after SCI, c-Met-IR was observed in GFAP-positive reactive astrocytes (J–L). Insets show magnified view. Scale bars = 200 μm in C (applies to A–C); 100 μm in F (applies to D–F); 200 μm in I (applies to G–I); 200 μm in L (applies to J–L).

tive histological analyses. First, the cavity area of the injured spinal cord at 6 weeks after SCI was obviously smaller in the HGF group than the LacZ group. Significant differences in the total cavity areas at the epicenter

and at 4 mm rostral and caudal to the epicenter were observed between the two groups (Fig. 4A). Second, the HGF group obviously had more preserved myelinated areas than the LacZ group at 6 weeks after SCI. Notably, the HGF group exhibited a significantly spared rim of white matter, even at the lesion epicenter, whereas the LacZ group exhibited severely demyelinated white matter throughout the lesion epicenter. Quantitative analysis of the myelinated areas revealed significant differences between the two groups at all of the examined sites (Fig. 4B). Next, to determine the effect of HGF on motoneurons, the numbers of ChAT-positive motoneurons in the ventral horns were quantified at 6 weeks after SCI. Although almost all the ChAT-positive motoneurons had disappeared at the lesion epicenter in both groups, significantly larger numbers of ChAT-positive motoneurons were observed at the site rostral to the epicenter in the HGF group compared with that in the LacZ group (Fig. 4C). These findings suggested that HGF exerted protective effects on motoneurons and oligodendrocytes and contributed to tissue sparing after SCI.

Next, to determine whether HGF inhibited the activation of caspase-3 after SCI, immunoblotting analyses using anti-cleaved caspase-3 antibody were performed at 1, 3, and 7 days after SCI. Cleaved caspase-3 was strongly induced after SCI and was most detectable at 3 days after SCI in both the HGF and the LacZ groups (Fig. 5A). Quantitative analysis revealed that the induction of cleaved caspase-3 was significantly attenuated in the HGF group compared with the LacZ group at 3 days after SCI (Fig. 5B). Furthermore, double immunostaining with anti-cleaved caspase-3 antibody and antibodies for neurons or oligodendrocytes showed that the numbers of NeuN and cleaved caspase-3 double-positive motoneurons in the ventral horns and GST-π and cleaved caspase-3 double-positive oligodendrocytes were
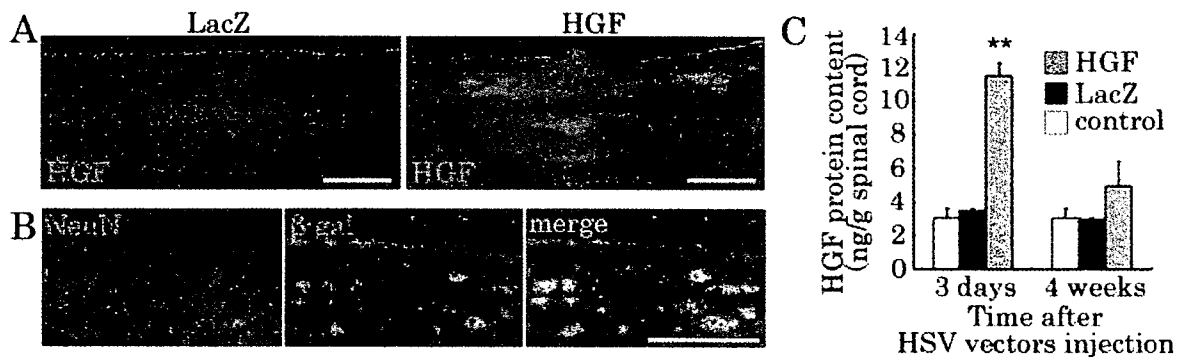

Fig. 3. Expression of exogenous HGF in the spinal cord introduced by HSV-HGF vector. Immunohistochemical staining of rat HGF in sagittal sections at 3 days after the HSV-1 vectors (HSV-HGF and HSV-LacZ) injection into the spinal cords showed remarkable HGF-IR in the extracellular matrix in the HGF group. In all the sagittal sections shown in the present study, the left side is the rostral side (A). β-Galactosidase expression was observed in neurons until 4 weeks after the HSV-LacZ injection

(B). HGF protein levels in 4-mm segments of spinal cords at the site of the HSV-1 vectors injection were analyzed using an ELISA at 3 days and 4 weeks after the injection. The HGF group showed a significantly larger amount of HGF protein than in intact spinal cord (control) and the LacZ group at 3 days after injection. No significant difference in the amount of HGF protein was seen among the three groups at 4 weeks after the injection (C). **P < 0.01; n = 3 each. Scale bars = 1 mm in A; 100 μm in B.
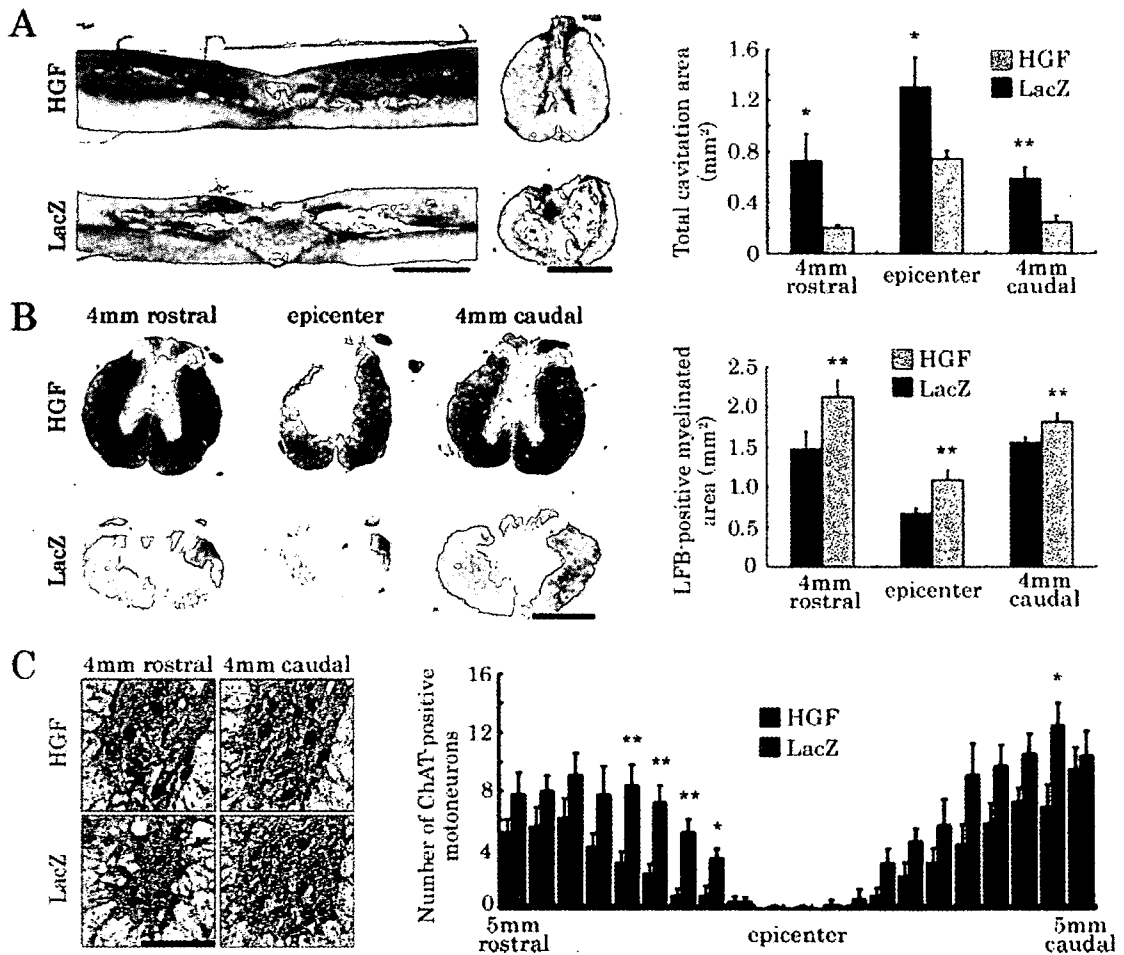
Fig. 4. Significant reduction in the size of damaged parenchyma in the HGF group. HE staining of midsagittal sections and the axial sections of lesion epicenter at 6 weeks after injury showed remarkably smaller areas of damage in the HGF group compared with the LacZ group. Significant differences in the total cavitation areas in the axial sections at the epicenter and at 4 mm rostral and caudal to the epicenter were observed between the two groups (n = 5 each; **A**). The axial sections stained with Luxol fast blue (LFB) at 6 weeks after injury showed a remarkable reduction in the area of demyelination in the HGF group compared with the LacZ group. Quantification of LFB-positive myelinated areas showed significant difference between the two groups at all of the examined sites (n = 5 each; **B**). The number of ChAT-positive motoneurons in the ventral horns at the lesion epicenter and adjacent sections up to 5 mm rostral and caudal to the epicenter in 0.5-mm increments was quantified at 6 weeks after SCI. The pictures show magnified views of right ventral horns of axial sections at 4 mm rostral and caudal to the epicenter. Significant differences between the two groups were observed mainly in the sections rostral to the epicenter (n = 5 each; **C**). $*P < 0.05$, $**P < 0.01$. Scale bars = 2 mm in A left; 1 mm in A right and B; 150 μm in C.
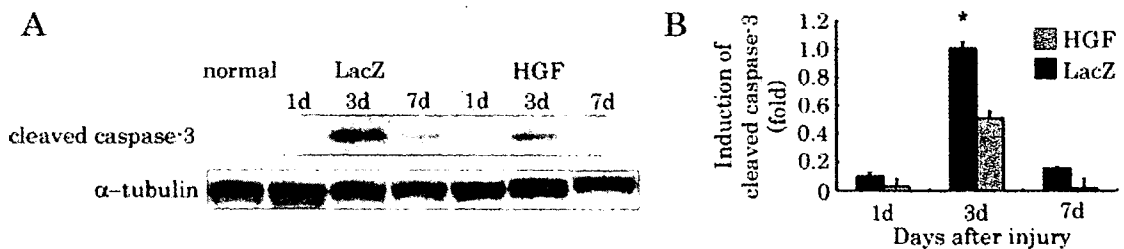

Fig. 5. Induction of cleaved caspase-3 in the injured spinal cord. Immunoblotting analyses showed remarkable induction of cleaved caspase-3 in the HGF and LacZ group during the acute phase of SCI, mainly at 3 days after SCI (**A**). Significantly attenuated cleaved caspase-3 induction was observed in the HGF group, compared with the LacZ group, at 3 days after SCI (n = 3 each; **B**). $*P < 0.05$.

obviously reduced in the HGF group compared with the LacZ group (data not shown). These results suggested that HGF significantly reduced the levels of cleaved caspase-3 activation in neurons and oligodendrocytes after SCI, thereby promoting their survival.

HGF Enhances Angiogenesis After SCI

To examine the effect of HGF on vascular endothelial cells after SCI, immunostaining with anti-RECA-1 antibody was performed. In intact thoracic spinal cord, the vessels had delicate walls composed of homogeneously stained endothelial cells. Although most of the vessels disappeared at the epicenter at 1 week after SCI, several vessels were stained intensely and showed abnormally large lumina with thick walls (Fig. 6A, arrows), which were not observed in the intact spinal cord. Quantitative MCID analysis of the RECA-1-positive areas showed significant differences at the epicenter and 4 mm rostral to the epicenter between the two groups (Fig. 6B). In these areas, there were large amounts of fragmented RECA-1-IR resulting from the debris of dead endothelial cells. Thus, we focused on RECA-1-positive vessels with intact lumina for quantitative analysis. Accordingly, we found that significant differences in the number of RECA-1-positive vessels with lumina larger than 20 μm, representing newly formed vessels (Casella et al., 2002), between the two groups at the epicenter and at 4 mm rostral to the epicenter at 1 week after SCI (Fig. 6C).

HGF Promotes Regrowth of Serotonergic Fibers and Functional Recovery After SCI

To determine the effects of HGF on the axonal growth after SCI, axial sections of injured spinal cords were immunostained with anti-5HT antibody at 1 week

and 6 weeks after SCI. 5HT-positive raphe-spinal serotonergic fibers were observed mainly in the gray matter in each group. Quantitative MCID analyses revealed that, whereas 5HT-positive fibers were almost undetectable in either group at 1 week after SCI, a significantly greater abundance of 5HT-positive fibers was detected, even in an area 4 mm caudal to the epicenter, in the HGF group compared with that in the LacZ group (Fig. 7A, arrows) at 6 weeks after SCI (Fig. 7A,B). Furthermore, at 1 week after SCI, the 5HT-positive fibers also showed c-Met-IR (Fig. 7C), and, at 6 weeks after SCI, they expressed GAP-43, which has been used as a marker of axonal regeneration (Kobayashi et al., 1997; Ramon-Cueto et al., 1998; Ikegami et al., 2005; Kaneko et al., 2006), even in a region 4mm caudal to the epicenter (Fig. 7D). Consistently with this, a greater abundance of GAP-43-positive fibers (Fig. 7E,F) and RT97-positive fibers (Fig. 7G,H) was observed, even in a region 4 mm caudal to the epicenter, in the HGF group compared with the LacZ group at 6 weeks after SCI; furthermore, c-Met-IR was also detected in these fibers (Fig. 7I,J). Most of the RT97-positive fibers were oriented longitudinally and parallel to each other (Fig. 7G), and these longitudinal fibers did not express GAP-43 (data not shown), indicating that they probably represented preserved axons after SCI.

The contusive SCI resulted in complete paralysis, followed by gradual recovery, reaching a plateau (BBB score 6.6 ± 1.1) at 6 weeks after SCI in the LacZ group. In the HGF group also, the animals suffered complete paralysis at 1 day after SCI, but these animals eventually showed better functional recovery than those in the LacZ group. Significant differences in the BBB scores were observed between the two groups from 7 days after SCI (Fig. 8). We believe that the difference between a BBB score of 8 (sweeping of hindlimbs) and
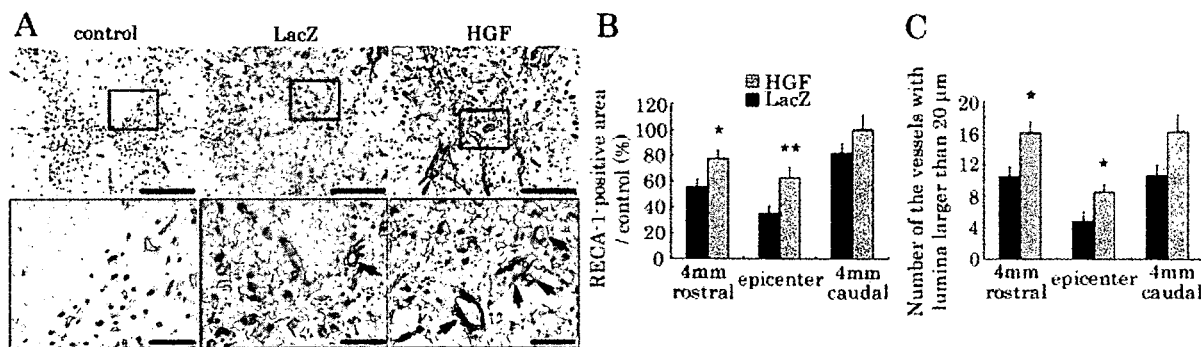

Fig. 6. Change in the microvasculature in the spinal cord after SCI. The axial sections of lesion epicenter at 1 week after SCI and intact thoracic spinal cord were immunostained with anti-RECA-1 antibody (A). Higher magnification views correspond to the boxed areas in the upper pictures. RECA-1-positive vessels with abnormally large lumina (arrows) emerged at 1 week after SCI in the two groups; these vessels were not observed in intact spinal cord and were consid-

ered to represent newly formed vessels after SCI. Quantitative analysis of the total area of RECA-1-positive endothelial cells (B) and the number of vessels with lumina larger than 20 μm (C) showed significant differences at the epicenter and at 4 mm rostral to the epicenter between the two groups. $*P < 0.05$, $**P < 0.01$; n = 5 each. Scale bars = 500 μm in A upper; 100 μm in A lower.
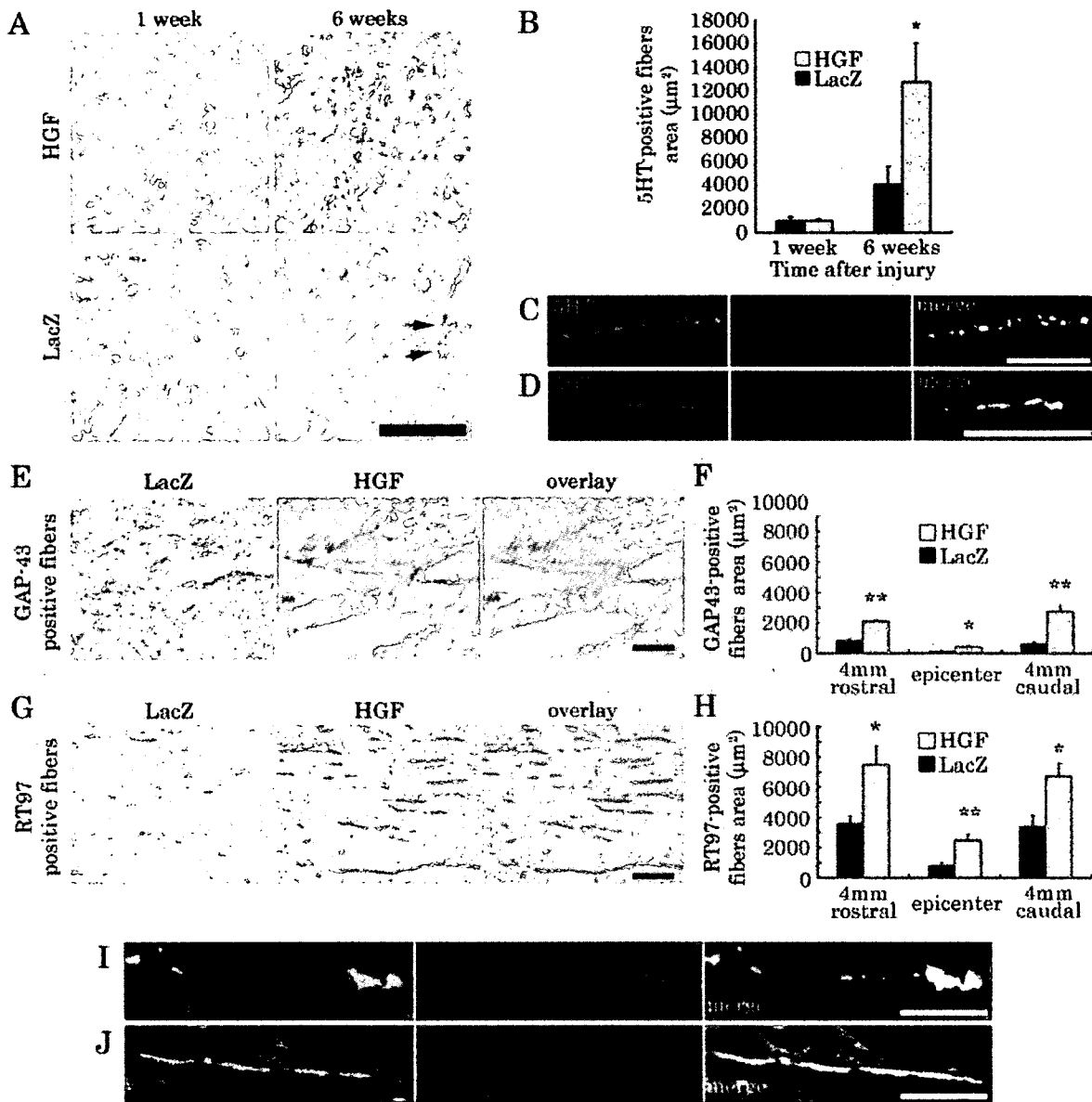
Fig. 7. Degeneration and regrowth of fibers after SCI. Immunostaining and quantification of 5-HT-positive fibers in axial sections at 4 mm caudal to the epicenter showed no significant difference between the two groups at 1 week after SCI but showed significant regrowth of the fibers in the HGF group compared with poor regrowth in the LacZ group (arrows) at 6 weeks after SCI (n = 5 each; **A,B**). 5HT-positive descending raphe-spinal fibers showed c-Met-IR (axial section) at 1 week after SCI (**C**) and expressed GAP-43 (sagittal section) at 4 mm caudal to the epicenter at 6 weeks after SCI (**D**). Representative images of midsagittal sections through an area 4 mm caudal to

the epicenter showed a significantly greater abundance of GAP-43-positive fibers (**E**) and R97-positive fibers (**G**) in the HGF group compared with that in the LacZ group at 6 weeks after SCI. Note that significant differences in the immunopositive area were observed even in the region 4 mm caudal to the epicenter between the two groups (n = 5 each; **F,H**). Double immunostaining of midsagittal sections at 1 week after SCI showed c-Met-IR in the GAP-43-positive growth cones (**I**) and RT97-positive neurofilaments (**J**). $*P < 0.05$. $**P < 0.01$. Scale bars = 50 µm in A,E,G,J; 20 µm in C,D; 10 µm in I.

a BBB score of 9 (weight support on hindlimbs) is clinically substantial. From a clinical perspective, the recovery of the HGF group to weight-supported plantar steps (BBB score 10.1 ± 0.6) was noteworthy.

DISCUSSION

Previous studies have shown that the HGF-c-Met system is involved in the mediation of inflammatory responses to tissue injury. In animal models in which the
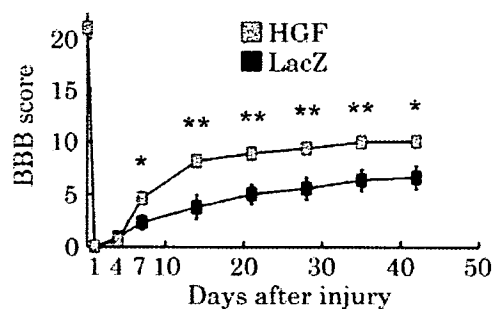
Fig. 8. BBB scores after SCI. A significant improvement in hindlimb motor function was observed in the HGF group compared with the LacZ group from 7 days after SCI (n = 14 each). $*P < 0.05$, $**P < 0.01$.

liver (Noji et al., 1990; Kono et al., 1992; Matsumoto and Nakamura, 1997), lung (Yanagita et al., 1993), or kidney (Kono et al., 1992; Igawa et al., 1993) tissues were experimentally damaged, the HGF mRNA expression and HGF activity were found to increase markedly in the damaged organs, peaking within 24 hr after the insult. Consistently with these increased expressions, the plasma HGF level also increased within 24 hr after the damage, suggesting that HGF could be delivered to these injured organs from other organs through the blood supply via an endocrine mechanism, in addition to being produced endogenously in these organs (Kono et al., 1992). In the CNS, on the other hand, it was reported that HGF mRNA was up-regulated exclusively in the periinfarct region at 14 days after cerebral ischemia (Nagayama et al., 2004). In the present study, we demonstrated for the first time that the HGF mRNA expression level gradually increased, peaking at 2 weeks after SCI, whereas the c-Met mRNA expression level increased markedly within 1 day of SCI. In addition, no increase in the plasma HGF levels was found after SCI. These findings suggest that the injured spinal cord cannot produce a sufficient amount of HGF by itself, compared with the remarkable increase in c-Met expression after SCI, nor can HGF be supplied through an endocrine mechanism, in contrast to the case following damage to other organs, as mentioned above. These results prompted us to perform an in vivo study to determine whether the application of exogenous HGF into the injured spinal cord might exert a beneficial effect and promote functional recovery in the spinal cord after SCI. We used the HSV-1 vector to introduce the exogenous HGF into the spinal cord, to compensate for the deficiency of endogenous HGF after SCI. The feasibility of using this vector for transgene expression in the nervous system in a safe and nontoxic manner has been examined in previous studies (Coffin et al., 1998; Palmer et al., 2000; Lilley et al., 2001).

We showed that the application of exogenous HGF into the injured spinal cord significantly attenuated caspase-3 activation in both neurons and oligodendrocytes, thereby reducing the area of demyelination and promoting the survival of cholinergic neurons. Previous

studies have demonstrated the neurotrophic effects of HGF on a variety of neurons (Hamanoue et al., 1996; Maina and Klein, 1999; Caton et al., 2000), and, in one study, the application of HGF prevented the apoptosis of adult motoneurons after axonotomy of the hypoglossal nerve (Okura et al., 1999). In addition, HGF overexpression was reported to prevent delayed neuronal death and decrease the infarct volume after cerebral ischemia (Miyazawa et al., 1998; Hayashi et al., 2001; Shimamura et al., 2004; Niimura et al., 2006) by attenuating apoptosis. Consistently with these reports, in the present study, the neurotrophic and antiapoptotic effects of HGF on the neurons prevented neuronal loss after SCI, thereby reducing the size of the damaged area. Oligodendrocyte death, which is mediated by a pathway involving caspase-11 and caspase-3, leads to demyelination (Hisahara et al., 2001), and inhibition of the apoptosis of oligodendrocytes has been shown to reduce the area of demyelination and functional impairment after SCI (Tamura et al., 2005). These reports indicate that the induction of apoptosis in oligodendrocytes is directly correlated with demyelination and that inhibition of the apoptosis of oligodendrocytes could be potentially beneficial for recovery after SCI. In the present study, we demonstrated that HGF markedly attenuated the induction of caspase-3 in the oligodendrocytes after SCI, resulting in a significant reduction in the area of demyelination after SCI. Taken together, the antiapoptotic and neurotrophic effects of HGF on the neurons and oligodendrocytes contributed to a significant reduction of the area of parenchymal damage after SCI.

HGF is also well known as a potent angiogenic factor. HGF and c-Met are known to be expressed in endothelial cells and vascular smooth muscle cells (VSMCs; Nakamura et al., 1995, 1996), and a relationship between improved microcirculation and behavioral recovery after cerebral ischemia has been suggested (Shimamura et al., 2004, 2006). A change in the microvasculature of the spinal cord after contusion injury has been shown to be essential for the ability of the spinal cord to undergo self-repair (Loy et al., 2002; Hagg and Oudega, 2006). The cordons of vessels that form early at the lesion site may be the initial stage of the trabeculae described in the contusion injury model; these trabeculae have been reported to promote endogenous repair and support axonal outgrowth in the injured spinal cord (Beattie et al., 1997). Loy and colleagues demonstrated a biphasic angiogenic response after SCI, the first phase of which (3–7 days after injury; Casella et al., 2002), but not the second (28–60 days after injury), corresponded to the time course of functional recovery (Loy et al., 2002). Moreover, a relationship between the blood flow and functional recovery has been shown following strategic treatments to improve angiogenesis in the injured spinal cord during the acute phase of SCI (Glaser et al., 2004; Guizar-Sahagun et al., 2005). Thus, enhancing the formation of blood vessels, especially during the acute phase of SCI, may be a potential repair strategy, because nutritional and mechanical support by vessels is critical

for axonal regeneration. Interestingly, the number, length, and diameter of the vessels have been reported to reach their maximum within 1 week after SCI, and vessels with abnormally large lumina may represent newly formed vessels after SCI (Casella et al., 2002). In the present study, we showed that the introduction of HGF into the injured spinal cord increased the total area of RECA-1-positive endothelial cells and number of vessels with abnormally large lumina by 1 week after SCI, confirming that HGF also promoted angiogenesis during the acute phase of SCI. Because HGF simultaneously stimulates the migration of endothelial cells and VSMCs (Nakamura et al., 1995, 1996), blood vessels might mature in a well-coordinated way, without the release of inflammatory cells (Morishita et al., 2004). Consistently with this suggestion, HGF overexpression reduced cerebral ischemic injury, without causing cerebral edema, through angiogenic and neuroprotective actions (Shimamura et al., 2004). Taken together, our results suggest that HGF may promote angiogenesis without enhancing blood vessel permeability after SCI and contribute to a reduction in the area of damage and regeneration of the injured spinal cord.

Several researchers have reported that HGF plays a role as an axonal chemoattractant and enhances the axonal growth of motoneurons (Ebens et al., 1996; Wong et al., 1997; Caton et al., 2000) and cortical neurons (Yamagata et al., 1995). Furthermore, it has been reported that overexpression of HGF in the chronic stage of cerebral infarction enhances neurite extension and increases the number of synapses, leading to improvements in learning and memory (Shimamura et al., 2006). In the present study, we demonstrated that HGF significantly induced the regrowth of raphe-spinal 5HT-positive fibers, which are known to contribute to the locomotor functions after SCI in rats (Bregman, 1987; Saruhashi et al., 1996; Kim et al., 2004; Kaneko et al., 2006), and the fibers expressed GAP-43 at 6 weeks after SCI. Moreover, c-Met-IR was also detected in the 5HT-positive fibers, suggesting that HGF directly acted on these fibers as well as the neuronal bodies to promote axonal regrwoth and recovery of locomotor functions after SCI. On the other hand, most of the longitudinal RT97-positive fibers oriented parallel to each other (Fig. 7G) did not express GAP-43 but expressed c-Met (Fig. 7J). Because these RT97-positive fibers were observed more abundantly in the HGF group than in the LacZ group at 6 weeks after SCI (Fig. 7H), it is likely that HGF protected the axons from degeneration.

Overall, during the acute phase of SCI, HGF appears to exert significant neuroprotective and antiapoptotic effects, to promote the survival of neurons and oligodendrocytes, and also to enhance angiogenesis around the lesion epicenter after SCI. These effects significantly reduced the area of damage and provided a better scaffold for axonal regeneration. Furthermore, HGF directly acted on the 5HT-positive fibers to promote their regrowth, which likely contributed to the significantly better recovery of the motor functions during the chronic phase of SCI. In conclusion, we have demonstrated that HGF exerted multiple beneficial effects on the injured spinal cord and significantly enhanced endogenous repair after SCI.

REFERENCES

Beattie MS, Bresnahan JC, Komon J, Tovar CA, Van Meter M, Anderson DK, Faden AI, Hsu CY, Noble LJ, Salzman S, Young W. 1997. Endogenous repair after spinal cord contusion injuries in the rat. Exp Neurol 148:453–463.

Blesch A, Tuszynski MH. 2001. GDNF gene delivery to injured adult CNS motor neurons promotes axonal growth, expression of the trophic neuropeptide CGRP, and cellular protection. J Comp Neurol 436:399–410.

Bottaro DP, Rubin JS, Faletto DL, Chan AM, Kmiecik TE, Vande Woude GF, Aaronson SA. 1991. Identification of the hepatocyte growth factor receptor as the c-met protooncogene product. Science 251:802–804.

Bregman BS. 1987. Spinal cord transplants permit the growth of serotonergic axons across the site of neonatal spinal cord transection. Brain Res 431:265–279.

Casella GT, Marcillo A, Bunge MB, Wood PM. 2002. New vascular tissue rapidly replaces neural parenchyma and vessels destroyed by a contusion injury to the rat spinal cord. Exp Neurol 173:63–76.

Caton A, Hacker A, Naeem A, Livet J, Maina F, Bladt F, Klein R, Birchmeier C, Guthrie S. 2000. The branchial arches and HGF are growth-promoting and chemoattractant for cranial motor axons. Development 127:1751–1766.

Coffin RS, Thomas SK, Thomas DP, Latchman DS. 1998. The herpes simplex virus 2 kb latency associated transcript (LAT) leader sequence allows efficient expression of downstream proteins which is enhanced in neuronal cells: possible function of LAT ORFs. J Gen Virol 79:3019–3026.

Date I, Takagi N, Takagi K, Kago T, Matsumoto K, Nakamura T, Takeo S. 2004. Hepatocyte growth factor improved learning and memory dysfunction of microsphere-embolized rats. J Neurosci Res 78:442–453.

Ebens A, Brose K, Leonardo ED, Hanson MG Jr, Bladt F, Birchmeier C, Barres BA, Tessier-Lavigne M. 1996. Hepatocyte growth factor/scatter factor is an axonal chemoattractant and a neurotrophic factor for spinal motor neurons. Neuron 17:1157–1172.

Glaser J, Gonzalez R, Perreau VM, Cotman CW, Keirstead HS. 2004. Neutralization of the chemokine CXCL10 enhances tissue sparing and angiogenesis following spinal cord injury. J Neurosci Res 77:701–708.

Grill R, Murai K, Blesch A, Gage FH, Tuszynski MH. 1997. Cellular delivery of neurotrophin-3 promotes corticospinal axonal growth and partial functional recovery after spinal cord injury. J Neurosci 17:5560–5572.

Guizar-Sahagun G, Ibarra A, Espitia A, Martinez A, Madrazo I, Franco-Bourland RE. 2005. Glutathione monoethyl ester improves functional recovery, enhances neuron survival, and stabilizes spinal cord blood flow after spinal cord injury in rats. Neuroscience 130:639–649.

Hagg T, Oudega M. 2006. Degenerative and spontaneous regenerative processes after spinal cord injury. J Neurotrauma 23:264–280.

Hamanoue M, Takemoto N, Matsumoto K, Nakamura T, Nakajima K, Kohsaka S. 1996. Neurotrophic effect of hepatocyte growth factor on central nervous system neurons in vitro. J Neurosci Res 43:554–564.

Hayashi K, Morishita R, Nakagami H, Yoshimura S, Hara A, Matsumoto K, Nakamura T, Ogihara T, Kaneda Y, Sakai N. 2001. Gene therapy for preventing neuronal death using hepatocyte growth factor: in vivo gene transfer of HGF to subarachnoid space prevents delayed neuronal death in gerbil hippocampal CA1 neurons. Gene Ther 8:1167–1173.

Hisahara S, Yuan J, Momoi T, Okano H, Miura M. 2001. Caspase-11 mediates oligodendrocyte cell death and pathogenesis of autoimmune-mediated demyelination. J Exp Med 193:111–122.

Igawa T, Matsumoto K, Kanda S, Saito Y, Nakamura T. 1993. Hepatocyte growth factor may function as a renotropic factor for regeneration in rats with acute renal injury. Am J Physiol 265:F61–F69.

Ikegami T, Nakamura M, Yamane J, Katoh H, Okada S, Iwanami A, Watanabe K, Ishii K, Kato F, Fujita H, Takahashi T, Okano HJ, Toyama Y, Okano H. 2005. Chondroitinase ABC combined with neural stem/progenitor cell transplantation enhances graft cell migration and outgrowth of growth-associated protein-43-positive fibers after rat spinal cord injury. Eur J Neurosci 22:3036–3046.

Jakeman LB, Wei P, Guan Z, Stokes BT. 1998. Brain-derived neurotrophic factor stimulates hindlimb stepping and sprouting of cholinergic fibers after spinal cord injury. Exp Neurol 154:170–184.

Kaneko S, Iwanami A, Nakamura M, Kishino A, Kikuchi K, Shibata S, Okano HJ, Ikegami T, Moriya A, Konishi O, Nakayama C, Kumagai K, Kimura T, Sato Y, Goshima Y, Taniguchi M, Ito M, He Z, Toyama Y, Okano H. 2006. A selective Sema3A inhibitor enhances regenerative responses and functional recovery of the injured spinal cord. Nat Med 12:1380–1389.

Kim JE, Liu BP, Park JH, Strittmatter SM. 2004. Nogo-66 receptor prevents raphespinal and rubrospinal axon regeneration and limits functional recovery from spinal cord injury. Neuron 44:439–451.

Kobayashi NR, Fan DP, Gichl KM, Bedard AM, Wiegand SJ, Tetzlaff W. 1997. BDNF and NT-4/5 prevent atrophy of rat rubrospinal neurons after cervical axotomy, stimulate GAP-43 and Talpha1-tubulin mRNA expression, and promote axonal regeneration. J Neurosci 17:9583–9595.

Kono S, Nagaike M, Matsumoto K, Nakamura T. 1992. Marked induction of hepatocyte growth factor mRNA in intact kidney and spleen in response to injury of distant organs. Biochem Biophys Res Commun 186:991–998.

Lilley CE, Groutsi F, Han Z, Palmer JA, Anderson PN, Latchman DS, Coffin RS. 2001. Multiple immediate-early gene-deficient herpes simplex virus vectors allowing efficient gene delivery to neurons in culture and widespread gene delivery to the central nervous system in vivo. J Virol 75:4343–4356.

Liu Y, Kim D, Himes BT, Chow SY, Schallert T, Murray M, Tessler A, Fischer I. 1999. Transplants of fibroblasts genetically modified to express BDNF promote regeneration of adult rat rubrospinal axons and recovery of forelimb function. J Neurosci 19:4370–4387.

Loy DN, Crawford CH, Darnall JB, Burke DA, Onifer SM, Whittemore SR. 2002. Temporal progression of angiogenesis and basal lamina deposition after contusive spinal cord injury in the adult rat. J Comp Neurol 445:308–324.

Maina F, Klein R. 1999. Hepatocyte growth factor, a versatile signal for developing neurons. Nat Neurosci 2:213–217.

Matsumoto K, Nakamura T. 1997. Hepatocyte growth factor (HGF) as a tissue organizer for organogenesis and regeneration. Biochem Biophys Res Commun 239:639–644.

Mautes AE, Weinzierl MR, Donovan F, Noble LJ. 2000. Vascular events after spinal cord injury: contribution to secondary pathogenesis. Phys Ther 80:673–687.

McTigue DM, Horner PJ, Stokes BT, Gage FH. 1998. Neurotrophin-3 and brain-derived neurotrophic factor induce oligodendrocyte proliferation and myelination of regenerating axons in the contused adult rat spinal cord. J Neurosci 18:5354–5365.

Miyazawa T, Matsumoto K, Ohmichi H, Katoh H, Yamashima T, Nakamura T. 1998. Protection of hippocampal neurons from ischemia-induced delayed neuronal death by hepatocyte growth factor: a novel neurotrophic factor. J Cereb Blood Flow Metab 18:345–348.

Morishita R, Aoki M, Hashiya N, Yamasaki K, Kurinami H, Shimizu S, Makino H, Takesya Y, Azuma J, Ogihara T. 2004. Therapeutic angiogenesis using hepatocyte growth factor (HGF). Curr Gene Ther 4:199–206.

Nagayama T, Nagayama M, Kohara S, Kamiguchi H, Shibuya M, Katoh Y, Itoh J, Shinohara Y. 2004. Post-ischemic delayed expression of hepatocyte growth factor and c-Met in mouse brain following focal cerebral ischemia. Brain Res 999:155–166.

Nakamura T, Nawa K, Ichihara A. 1984. Partial purification and characterization of hepatocyte growth factor from serum of hepatectomized rats. Biochem Biophy Res Commun 122:1450–1459.

Nakamura T, Nishizawa T, Hagiya M, Seki T, Shimonishi M, Sugimura A, Tashiro K, Shimizu S. 1989. Molecular cloning and expression of human hepatocyte growth factor. Nature 342:440–443.

Nakamura Y, Morishita R, Higaki J, Kida I, Aoki M, Moriguchi A, Yamada K, Hayashi S. Yo Y, Matsumoto K, et al. 1995. Expression of local hepatocyte growth factor system in vascular tissues. Biochem Biophys Res Commun 215:483–488.

Nakamura Y, Morishita R, Nakamura S, Aoki M, Moriguchi A, Matsumoto K, Nakamura T, Higaki J, Ogihara T. 1996. A vascular modulator, hepatocyte growth factor, is associated with systolic pressure. Hypertension 28:409–413.

Niimura M, Takagi N, Takagi K, Mizutani R, Ishihara N, Matsumoto K, Funakoshi H, Nakamura T, Takeo S. 2006. Prevention of apoptosis-inducing factor translocation is a possible mechanism for protective effects of hepatocyte growth factor against neuronal cell death in the hippocampus after transient forebrain ischemia. J Cereb Blood Flow Metab (in press).

Noji S, Tashiro K, Koyama E, Nohno T, Ohyama K, Taniguchi S, Nakamura T. 1990. Expression of hepatocyte growth factor gene in endothelial and Kupffer cells of damaged rat livers, as revealed by in situ hybridization. Biochem Biophys Res Commun 173:42–47.

Okura Y, Arimoto H, Tanuma N, Matsumoto K, Nakamura T, Yamashima T, Miyazawa T, Matsumoto Y. 1999. Analysis of neurotrophic effects of hepatocyte growth factor in the adult hypoglossal nerve axotomy model. Eur J Neurosci 11:4139–4144.

Palmer JA, Branston RH, Lilley CE, Robinson MJ, Groutsi F, Smith J, Latchman DS, Coffin RS. 2000. Development and optimization of herpes simplex virus vectors for multiple long-term gene delivery to the peripheral nervous system. J Virol 74:5604–5618.

Ramon-Cueto A, Plant GW, Avila J, Bunge MB. 1998. Long-distance axonal regeneration in the transected adult rat spinal cord is promoted by olfactory ensheathing glia transplants. J Neurosci 18:3803–3815.

Saruhashi Y, Young W, Perkins R. 1996. The recovery of 5-HT immunoreactivity in lumbosacral spinal cord and locomotor function after thoracic hemisection. Exp Neurol 139:203–213.

Shimamura M, Sato N, Oshima K, Aoki M, Kurinami H, Waguri S, Uchiyama Y, Ogihara T, Kaneda Y, Morishita R. 2004. Novel therapeutic strategy to treat brain ischemia: overexpression of hepatocyte growth factor gene reduced ischemic injury without cerebral edema in rat model. Circulation 109:424–431.

Shimamura M, Sato N, Waguri S, Uchiyama Y, Hayashi T, Iida H, Nakamura T, Ogihara T, Kaneda Y, Morishita R. 2006. Gene transfer of hepatocyte growth factor gene improves learning and memory in the chronic stage of cerebral infarction. Hypertension 47:742–751.

Sun W, Funakoshi H, Matsumoto K, Nakamura T. 2000. A sensitive quantification method for evaluating the level of hepatocyte growth factor and c-met/HGF receptor mRNAs in the nervous system using competitive RT-PCR. Brain Res Brain Res Protoc 5:190–197.

Tamura M, Nakamura M, Ogawa Y, Toyama Y, Miura M, Okano H. 2005. Targeted expression of anti-apoptotic protein p35 in oligodendrocytes reduces delayed demyelination and functional impairment after spinal cord injury. Glia 51:312–321.

Tuszynski MH, Peterson DA, Ray J, Baird A, Nakahara Y, Gage FH. 1994. Fibroblasts genetically modified to produce nerve growth factor induce robust neuritic ingrowth after grafting to the spinal cord. Exp Neurol 126:1–14.

Tuszynski MH, Gabriel K, Gage FH, Suhr S, Meyer S, Rosetti A. 1996. Nerve growth factor delivery by gene transfer induces differential outgrowth of sensory, motor, and noradrenergic neurites after adult spinal cord injury. Exp Neurol 137:157–173.

Vavrek R, Girgis J, Tetzlaff W, Hiebert GW, Fouad K. 2006. BDNF promotes connections of corticospinal neurons onto spared descending interneurons in spinal cord injured rats. Brain 129:1534–1545.

Wong V, Glass DJ, Arriaga R, Yancopoulos GD, Lindsay RM, Conn G. 1997. Hepatocyte growth factor promotes motor neuron survival and synergizes with ciliary neurotrophic factor. J Biol Chem 272:5187–5191.

Yamagata T, Muroya K, Mukasa T, Igarashi H, Momoi M, Tsukahara T, Arahata K, Kumagai H, Momoi T. 1995. Hepatocyte growth factor specifically expressed in microglia activated Ras in the neurons, similar to the action of neurotrophic factors. Biochem Biophys Res Commun 210:231–237.

Yanagita K, Matsumoto K, Sekiguchi K, Ishibashi H, Niho Y, Nakamura T. 1993. Hepatocyte growth factor may act as a pulmotrophic factor on lung regeneration after acute lung injury. J Biol Chem 268:21212–21217.

Zhao MZ, Nonoguchi N, Ikeda N, Watanabe T, Furutama D, Miyazawa D, Funakoshi H, Kajimoto Y, Nakamura T, Dezawa M, Shibata MA, Otsuki Y, Coffin RS, Liu WD, Kuroiwa T, Miyatake S. 2006. Novel therapeutic strategy for stroke in rats by bone marrow stromal cells and ex vivo HGF gene transfer with HSV-1 vector. J Cereb Blood Flow Metab 26:1176–1188.

Development/Plasticity/Repair

In Vivo Tracing of Neural Tracts in the Intact and Injured Spinal Cord of Marmosets by Diffusion Tensor Tractography

Kanehiro Fujiyoshi,[1,2]* Masayuki Yamada,[4,5]* Masaya Nakamura,[1] Junichi Yamane,[1,2] Hiroyuki Katoh,[1] Kazuya Kitamura,[1,2] Kenji Kawai,[4] Seiji Okada,[6] Suketaka Momoshima,[3] Yoshiaki Toyama,[1] and Hideyuki Okano[2]

Department of [1]Orthopaedic Surgery, [2]Physiology, and [3]Radiology and [4]Center for Integrated of Medical Research, Keio University School of Medicine, Shinjuku, Tokyo 160-8582, Japan, [5]Central Institute for Experimental Animals, Miyamae-ku, Kawasaki, Kanagawa 216-0001, Japan, and [6]Department of Research Superstar Program Stem Cell Unit, Graduate School of Medical Science, Kyushu University, Fukuoka 812-8582, Japan

In spinal cord injury, axonal disruption results in motor and sensory function impairment. The evaluation of axonal fibers is essential to assess the severity of injury and efficacy of any treatment protocol, but conventional methods such as tracer injection in brain parenchyma are highly invasive and require histological evaluation, precluding clinical applications. Previous advances in magnetic resonance imaging technology have led to the development of diffusion tensor tractography (DTT) as a potential modality to perform *in vivo* tracing of axonal fibers. The properties and clinical applications of DTT in the brain have been reported, but technical difficulties have limited DTT studies of the spinal cord. In this study, we report the effective use of DTT to visualize both intact and surgically disrupted spinal long tracts in adult common marmosets. To verify the feasibility of spinal cord DTT, we first performed DTT of postmortem marmosets. DTT clearly illustrated spinal projections such as the corticospinal tract and afferent fibers in control animals, and depicted the severed long tracts in the injured animals. Histology of the spinal cords in both control and injured groups were consistent with DTT findings, verifying the accuracy of DTT. We also conducted DTT in live marmosets and demonstrated that DTT can be performed in live animals to reveal *in vivo* nerve fiber tracing images, providing an essential tool to evaluate axonal conditions in the injured spinal cord. Taken together, these findings demonstrate the feasibility of applying DTT to preclinical and clinical studies of spinal cord injury.

Key words: spinal cord injury; corticospinal tract; diffusion tensor tractography; magnetic resonance imaging; common marmoset; calmodulin-dependent protein kinase II-α; pathway-specific DTT; *in vivo* tracing

Introduction

We established previously a reproducible spinal cord injury (SCI) model in adult common marmosets and demonstrated that transplantation of human neural stem/progenitor cells into the injured spinal cord promoted functional recovery (Iwanami et al., 2005b). An increase of axonal fibers, evaluated through histological methods, was observed near the transplanted neural stem/progenitor cells and were interpreted to be involved in the functional improvement. Such evaluation of axonal fibers is essential to assess the severity of SCI and efficacy of any treatment protocol (Olson, 2002; Kaneko et al., 2007), but conventional methods such as tracer injection in brain parenchyma are technically demanding and highly invasive (Ralston and Ralston, 1985; Lacroix et al., 2004). Because histological examinations are

required to evaluate tracer studies, it has been impossible to evaluate axonal fibers *in vivo* and follow the sequential growth of axonal fibers in the same animal. Understanding the value of such an examination method, we therefore sought to establish a noninvasive method to evaluate axonal fibers *in vivo*.

Magnetic resonance imaging (MRI) is essential for predicting prognosis and planning the treatment of patients with SCI (Kulkarni et al., 1987; Yamashita et al., 1990). Our previous study using common marmosets also demonstrated that MRI could detect pathological changes after SCI (Iwanami et al., 2005a). However, the information provided by conventional T1- and T2-weighted MRI of the spinal cord is essentially limited to the differentiation of the white matter from the gray matter. Conventional MRI depicts the white matter as a uniform tissue, although it actually contains a complex array of directionally oriented nerve fibers. Methods to visualize the pathways of the white matter *in vivo* have been long sought and, recently, diffusion tensor tractography (DTT) has demonstrated this ability (Ito et al., 2002; Masutani et al., 2003; Mori et al., 2003).

Diffusion tensor imaging (DTI) is a new imaging technique that takes advantage of the anisotropic nature of water diffusion in biological tissue to obtain detailed microstructural information (Le Bihan et al., 1986; Moseley et al., 1990; Basser et al., 1994; Beaulieu, 2002; Mori and Zhang, 2006). By analyzing and reconstructing that data obtained by DTI, DTT can follow the orienta-

Figure 1. DTT of the intact spinal cord in a postmortem common marmoset. *A*, Coronal T2-weighted MRI. *B*, *C*, Full-width DTT of the spinal cord (*B*) and an axial section (*C*) superimposed on axial T2-weighted images. The ROI was placed in the lower cervical spinal cord and DTT was traced in the cranial direction. DTT tracts are color coded to indicate tract orientation: red for left–right orientation, green for anterior–posterior orientation, and blue for superior–inferior orientation. *D*, *E*, Directionally color-coded axial FA map of the spinal cord (*D*) reveals that the configuration of the white matter depicted in blue is consistent with the myelin-positive area in an axial section of the same area stained with LFB (*E*). *C–E* are axial images of the C5/6 level (*B*, arrow). Scale bar, 1 mm.

tion of nerve fibers to trace specific neural pathways such as the corticospinal tract (CST) in the brain (Conturo et al., 1999; Masutani et al., 2003; Kamada et al., 2005a; Lee et al., 2005). Compared with the brain, however, DTT of the spinal cord is more difficult because of its smaller size and *in vivo* bulk motion (Basser and Jones, 2002; Maier and Mamata, 2005; Kharbanda et al., 2006). Several researchers have reported previously on successful DTT of the human spinal cord (Holder et al., 2000; Facon et al., 2005; Tsuchiya et al., 2005; Ducreux et al., 2006). However, because these DTT images were not confirmed with detailed histological studies, whether DTT actually reflects the anatomical axonal fibers remains unclear. In this study, we performed DTT of both intact and injured spinal cords in common marmosets and confirmed the accuracy of DTT through histology.

Materials and Methods

Hemisection SCI in common marmoset. Adult female common marmosets (266–384 g; Clea Japan, Tokyo, Japan) were used in the present study (*n* = 6). All interventions and animal care procedures were performed in accordance with the Laboratory Animal Welfare Act, the *Guide for the Care and Use of Laboratory Animals* (National Institutes of Health), and the *Guidelines and Policies for Animal Surgery* provided by the Animal Study Committee of the Central Institute for Experimental Animals of Keio University, and were approved by the ethics committee of Keio University. All surgeries were performed under general anesthesia induced by intramuscular injection of ketamine (50 mg/kg; Sankyo, Tokyo, Japan) and xylazine (5 mg/kg; Bayer, Leverkusen, Germany) and maintained by isoflurane (Foren; Abbott, Tokyo, Japan). The animal's pulse, arterial oxygen saturation, and rectal temperature were monitored during the surgical procedures. After a laminectomy at the C6 level, the dura mater was opened longitudinally and the right side of the spinal cord was cut at the C6 level using a surgical scalpel in the hemisection group (*n* =

3). The control group in this study in was a naive control without any surgical intervention.

Magnetic resonance imaging. MRI was performed using a 7.0 tesla MRI, PharmaScan 70/16 (BioSpin; Bruker) with a coil dedicated for small animals. In the studies using postmortem animals (control and hemisection groups, *n* = 2 each), conventional T2-weighted images (T2WIs) were first obtained, followed by intracardiac perfusion with 4% paraformaldehyde (PFA), pH 7.4, and diffusion tensor MRI. T2WI and diffusion tensor MRI of the hemisected animals were conducted 2 weeks after injury. DTI data sets were acquired with a spin-echo sequence based on the Stejskal–Tanner diffusion preparation. Scanning parameters were as follows: repetition time (TR), 15000 ms; echo time (TE), 40 ms; flip angle, 90°, field of view (FOV), 55 × 55 mm; acquisition data matrix, 256 × 256; reconstructed image resolution, 0.215 mm (with zero-filling interpolation); slice thickness, 0.85 mm; b-value, 1000 s/mm^2; motion-probing gradient (MPG) orientations, 12 axes; number of averaging (NA), 1. In the studies using live animals (control and hemisection group, *n* = 1 each), conventional and diffusion tensor MRI were performed under the general anesthesia as mentioned above. MRI scans of the hemisected animal were conducted 2 weeks after injury. In live animals, to reduce motion artifacts from the blood flow and CSF flow, animals were immobilized on an acrylic bed with a specially designed head positioner and electrocardiogram (ECG) probe (SA Instruments) for gated imaging was attached to the animal's front thorax. DTI data sets in live animals were acquired with an ECG-gated standard diffusion weighted spin-echo pulse sequence based on the Stejskal–Tanner diffusion preparation (Stejskal and Tanner, 1965). Scanning parameters were as follows: TR, 3500 ms; TE, 40 ms; flip angle, 90°; FOV, 40 × 40 mm; acquisition data matrix, 128 × 128; reconstructed image resolution, 0.31 × 0.31 mm; slice thickness, 0.94 mm; b-value, 1000 s/mm^2; MPG orientations, 12 axes; NA, 1.

Diffusion tensor analysis. Diffusion tensor and three-dimensional analysis were performed using Volume One and dTV IISR software (Kuni-
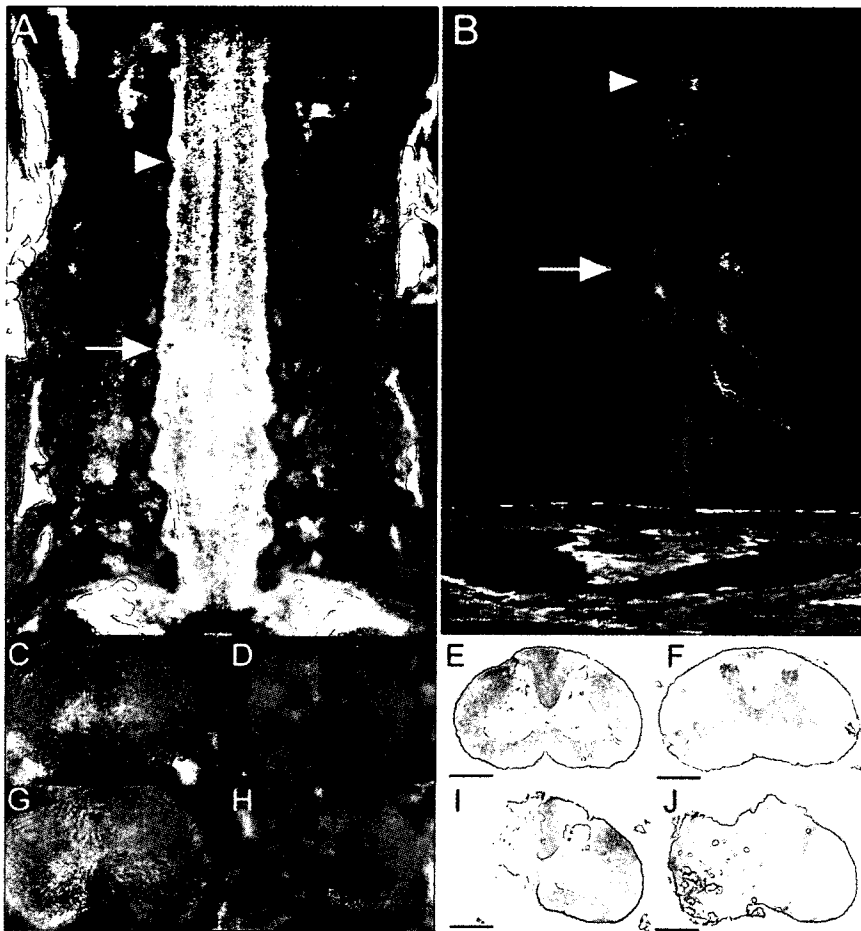
Figure 2. DTT of the hemisected spinal cord at 2 weeks after injury in a postmortem common marmoset. *A*, Coronal T2-weighted MRI depicted the hemisection injury as a low-intensity area with no change in the cord caudal to the injury. *B*, DTT of the hemisected spinal cord. The ROI was placed in the upper cervical spinal cord, and DTT was traced in the caudal direction revealing disruption of white matter fibers on the hemisected side. The traced tracts became untraceable at the injury site, whereas tracts on the contralateral side continued caudally. Arrows indicated the hemisection site and arrowheads indicated the point 8 mm cranial to the injury site in *A* and *B*. *C–J*, DTT (*C, G*), FA map (*D, H*), LFB staining (*E, I*), and HE staining (*F, J*) of the spinal cord 8 mm cranial to the injury site (*C–F*) and at the hemisection site (*G–J*). Although normal FA and anatomy of the spinal cord was confirmed cranial to the hemisection site, there was a significant decrease in FA of the white matter fibers at the hemisection site (*G, H*). Consistent with these changes in DTT (*G*) and color-coded FA map (*H*), demyelination was seen at the hemisection site (*I*). Scale bars, 1 mm.

diffusion tensor MRI and then the spinal cord tissues were removed. All spinal cord specimens were postfixed in 4% PFA and immersed overnight in 10% sucrose followed by 30% sucrose. Frozen section blocks were prepared and cut into 20-μm-thick axial sections using a cryostat. These sections were stained with hematoxylin-eosin (HE) for general histological examinations and Luxol fast blue (LFB) for evaluation of the myelinated area. Immunostaining with anti-CaMKII-α antibody (primary antibody, diluted 1:100, mouse monoclonal; Zymed, San Francisco, CA; secondary antibody, a biotin-labeled goat anti-mouse IgG for ABC and DAB staining) was performed to examine the CST.

Results

DTT of intact and injured spinal cords in postmortem common marmosets

Based on the data from *in vivo* high-resolution diffusion tensor MR images of postmortem common marmoset spinal cords (Fig. 1A), we created a DTT of the cervical spinal cord that enabled us to detect various fibers of the spinal cord (Fig. 1B). In a color-coded DTT of the intact cervical spinal cord, each path traced by DTT, which we will refer to have as a tract, is depicted in colors according to its orientation (Pajevic and Pierpaoli, 1999): red for left–right orientation, green for anterior–posterior orientation, and blue for superior–inferior orientation (Fig. 1B,C). White matter fibers with high craniocaudal diffusion anisotropy were visible in blue on color-coded maps of fractional anisotropy (FA) (Basser and Pierpaoli, 1996), an index of anisotropy ranging from 0 (perfectly isotropic diffusion) to 1 (a hypothetical infinite cylinder), which had been calculated from the same data (Fig. 1D) and the distribution of longitudinal fibers was consistent with the distribution of myelinated axons stained with LFB (Fig. 1E). In the gray matter, horizontal fibers passing from the central canal to the anterior horn of the spinal cord were observed in red, but almost no diffusion anisotropy was detected in the remaining gray matter, which is mainly occupied by neuronal and glial cells.

In the marmosets with hemisected spinal cords, the hemisected area of spinal cord appeared as a high-intensity area in coronal T2WIs 2 weeks after injury (Fig. 2A). DTT of the hemisected spinal cord revealed that the longitudinal fibers of the white matter in the injured side were disrupted at the hemisection site, but preserved in the intact side (Fig. 2B). In axial DTT images and color-coded FA maps, there was a significant decrease in FA of the longitudinal fibers of the white matter as well as the transverse fibers of the gray matter at the hemisection site (Fig. 2G,H), compared with the site 8 mm cranial to the hemisection site (Fig. 2C,D). Consistent with these changes in DTT and colored FA maps, histology of the hemisected area revealed disruption of both gray and white matter with severe demyelination. (Fig. 2I,J).

matsu et al., 2003; Masutani et al., 2003). An eigenvector (e1) associated with the largest eigenvalue (λ1) was assumed to represent the local fiber direction. Fiber tracking was initiated from a manually selected region of interest (ROI) area, which is the "seed" from which tracking lines were propagated bidirectionally according to the eigenvector (e1) at each voxel pixel. The direction of diffusion anisotropy was followed until tracking was terminated when it reached a voxel with a fractional anisotropy of <0.25. To delineate the motor tracts, the seed was placed on the area histologically known to contain CaMKII-α-positive fibers in the upper cervical cord, which corresponds to the CST (Terashima et al., 1994; Iwanami et al., 2005a). To delineate the afferent pathways of the spinal cord, we placed the seed at the anterolateral and posterior funiculi of the lower cervical cord, which correspond to the spinothalamic tract and the gracile fasciculus, respectively. We used the two-regions-of-interest method (Mori et al., 2003), which consists of seed and target regions to depict the pyramidal decussation from the medullary pyramid (seed) to the opposite CST area in the upper cervical cord (target).

Histological analyses. In the postmortem group, spinal cord tissues were removed after diffusion tensor MRI. In the live group, each animal was perfused intracardially with 4% paraformaldehyde after

Pathway-specific DTT in postmortem common marmosets

To examine the feasibility of visualizing individual pathways in common marmosets, we analyzed the CST from the medulla to the upper cervical spinal cord because the course of the CST in this region is unique and well known. Analysis of histological sections stained for calmodulin-dependent protein kinase II-α (CaMKII-α) determined the location of the CST (Terashima et al., 1994; Iwanami et al., 2005a) within the medulla, and DTT of the CST was performed by setting the ROI, which is a manually selected area based on anatomical knowledge from which DTT fiber tracking was initiated, in the pyramid of the medulla and tracing caudally (Fig. 3A). The course of the CST in this area has been well documented in the literature; the majority of fibers cross to the contralateral side through the pyramidal decussation and descended the lateral funiculus (lateral CST), whereas a small group of fibers descend the ipsilateral anterior (anterior CST) and lateral funiculus (anterolateral CST) (Qiu et al., 1991; Lacroix et al., 2004; Lemon et al., 2004). A study in humans demonstrated the composition of the CST, with the lateral CST accounting for 90% of CST fibers and the anterior CST and uncrossed lateral CST accounting for the remaining 8 and 2%, respectively (Carpenter and Sutin, 1983). DTT was capable of tracing fibers through all three courses and successfully demonstrated the pyramidal decussation of the CST (Fig. 3B–E). However the number of tracts depicted with DTT through each course did not reflect the amount of CST fibers traveling through each pathway, because the number of DTT tracts depicted descending each pathway were similar although a majority of CST fibers actually travel through the lateral CST.

We focused on the pyramidal decussation of the CST and conducted histological studies to verify the results of DTT. DTT and histological sections from similar points along the craniocaudal axis were compared. The course of the CST depicted by DTT (Fig. 3H) corresponded to the area positive for CaMKII-α (Fig. 3I), which recognizes fibers of the CST, and LFB staining of the same section (Fig. 3J) confirmed that the CST delineated by DTT and CaMKII-α contained myelinated fibers. CST-specific DTT superimposed on MR images verified that the pyramidal decussation was depicted in the proper position (Fig. 3F,G).

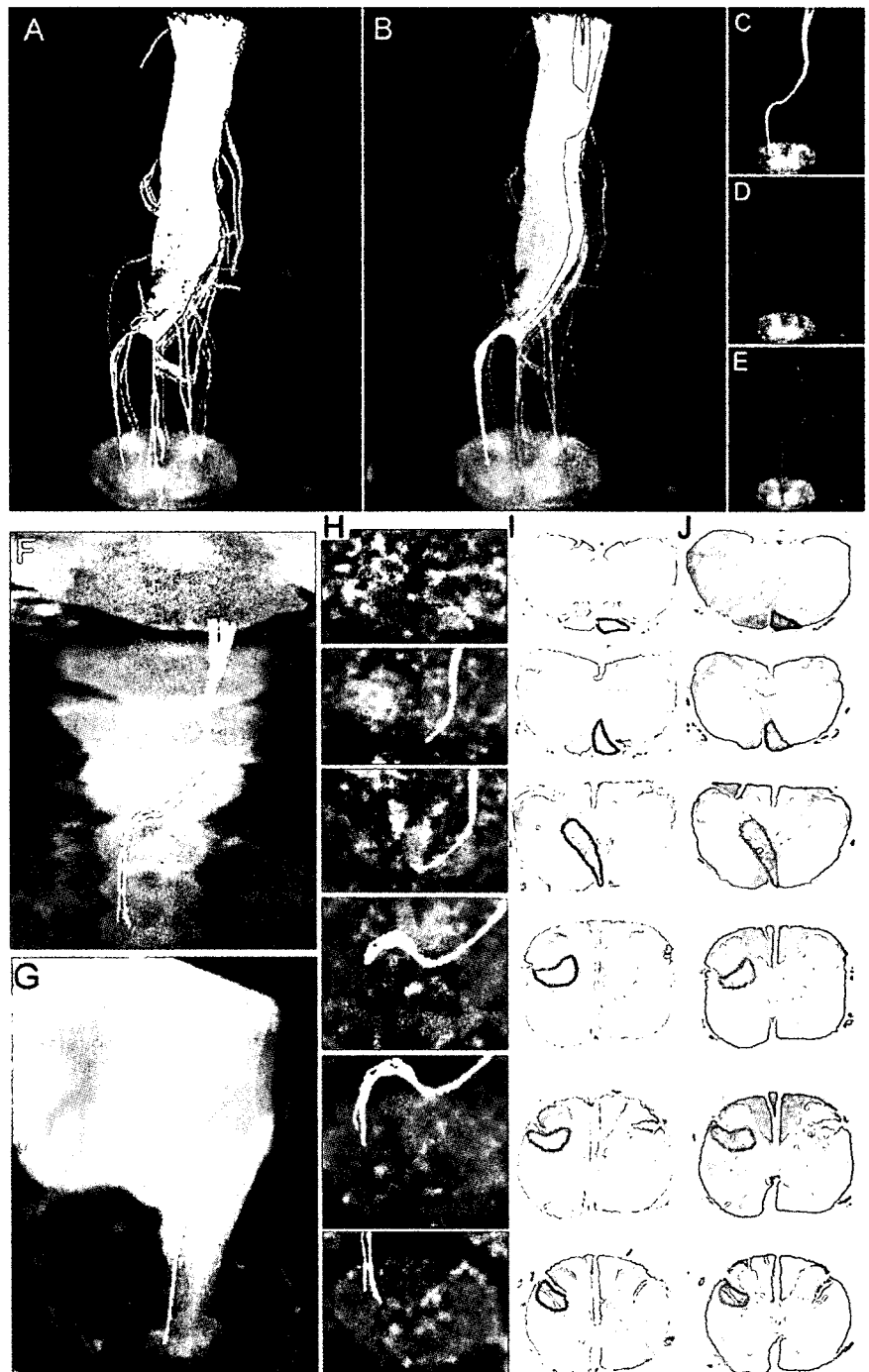With sufficient data to indicate that CST-specific DTT is possible, we then con-

Figure 3. Pathway-specific DTT in a postmortem common marmoset revealing the course of the corticospinal tract with pyramidal decussation. **A**, DTT of the CST was conducted by placing the ROI in the pyramid of the medulla and tracing caudally. Note that the volume of traced tracts decrease as the tracing was carried caudally, because many tracts became untraceable because of the partial volume effect. **B**, By placing secondary ROIs in areas of the upper cervical spinal cord known to contain CST fibers, CST fibers that pass through both ROIs could be depicted. **C**, Lateral CST fibers that crossed over to and descended the contralateral lateral funiculus in a pattern suggesting pyramidal decussation were depicted in yellow. **D**, Uncrossed lateral fibers descending the ipsilateral lateral funiculus were depicted in red. **E**, Lateral fibers descending the ipsilateral anterior funiculus were depicted in blue. The fact that DTT was capable of accurately depicting all three known pathways of the CST is significant. However, it is important to note that the depicted DTT tracts do not accurately reflect the volume of nerve fibers, because it is known that the lateral CST contains the majority of CST fibers. **F, G**, DTT of the pyramidal decussation superimposed on three-dimensional MR images to macroscopically confirm that the pyramidal decussation was depicted in the proper height in the medulla and the upper cervical cord, using the cerebellum as a reference point. **H**, DTT of the pyramidal decussation superimposed on axial color-coded FA maps. **I, J**, Axial histological slices of the same points in **H** stained for CaMKII-α to reveal the location of CST fibers (**I**) and LFB to delineate the configuration of the white matter (**J**). In each slice, the area through which the DTT CST tract passes was positive for CaMKII-α and LFB, confirming the accuracy of DTT.
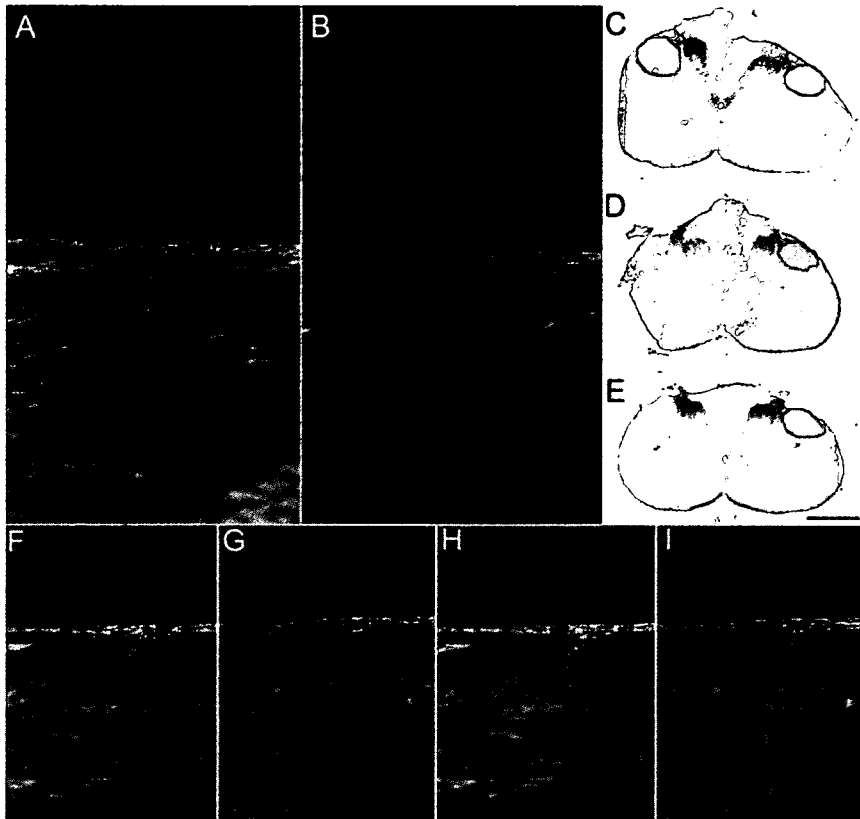
Figure 4. *In vivo* CST- and afferent pathway-specific DTT of intact and injured spinal cords in postmortem common marmosets. *A*, DTT of an intact CST superimposed on a color-coded FA map of the C5/6 level. *B*, DTT of the CST in a hemisected spinal cord superimposed on a color-coded FA map of the hemisected C5/6 level 2 weeks after injury revealing disruption of the CST at the site of injury. *C–E*, CaMKII-α staining of an axial section of the hemisected spinal cord 8 mm cranial to the hemisection site (*C*), at the hemisection site (*D*), and 8 mm caudal to the hemisection site (*E*). Because CaMKII-α is a known substance transported in the axons of the CST, the absence of CaMKII-α staining distal to the injury suggested CST disruption, confirming the results of CST-specific DTT. *F, H,* In the control group, ROI was placed at the anterolateral funiculus (*F*) or the posterior funiculus (*H*), and a DTT of the afferent pathways was drawn in the caudocranial direction. *G, I,* In the hemisection group, no fibers were observed at the site rostral to the hemisection site, demonstrating that tract-specific DTT can potentially delineate the spinothalamic tract (*G*) and dorsal column-medial lemniscus pathway (*I*). Scale bar, 1 mm.

ducted CST-specific DTT of hemisected spinal cords to observe how DTT would depict an injured pathway. CST-specific DTTs of the middle to lower cervical spinal cord were compared in intact and hemisected postmortem common marmosets. In the intact cervical spinal cord, DTT depicted descending CST tracts in the bilateral lateral funiculus (Fig. 4D). In the hemisected cervical spinal cord 2 weeks after injury, FA decreased in color-coded FA maps and no tracts were found caudal to the hemisection site on the injured side whereas the intact CST pathway was observed descending the uninjured side (Fig. 4B). Histology confirmed the disruption of the CST at the hemisection site with robust CaMKII-α staining rostral to the hemisection (Fig. 4C) and no CaMKII-α positive CST fibers at and caudal to the hemisection site (Fig. 4D,E).

Using a similar technique, it is also possible to trace pathways other than the CST. By placing the ROI in areas known to contain afferent fibers and tracing in the caudocranial direction, the spinothalamic tract in the anterolateral funiculus (Fig. 4F) and the medial lemniscus pathway in the posterior funiculus (Fig. 4B) were depicted. When the same procedure was repeated in the hemisected group, the ascending tracts were disrupted at the hemisection site with no tracts rostral to the lesion on the injured

side, whereas normal ascending tracts were observed in the uninjured side (Fig. 4G,I).

Pathway-specific DTT of intact and injured spinal cords in live common marmosets

To evaluate the clinical feasibility of DTT, we repeatedly performed *in vivo* pathway-specific DTT on live animals and compared the results with those obtained from postmortem animals. Similar to the DTT of postmortem animals, *in vivo* DTT of the intact cervical CST in live animals showed longitudinal tracts in the lateral funiculus bilaterally (Fig. 5B), and pathway-specific DTT of afferent fibers depicted tracts in the anterolateral and posterior funiculus (Figs. 5C,D). In the hemisected marmoset 2 weeks after injury, T2WI MRI revealed a low-intensity area at the hemisection site and a high-intensity area at the same level on the intact side (Fig. 5E), whereas DTT showed disruption of the CST (Fig. 5F) and ascending fibers at the lesion site (Fig. 5G,H). Pathway-specific *in vivo* DTT findings in live animals were highly similar to those of postmortem animals, especially in major tract morphology. Because MRI scans of live animals required anesthesia, the scan duration and, therefore, scan area were considerably limited compared with postmortem animals; MRIs of live animals were conducted in 1.5 h whereas 10 h scans were performed for postmortem animals. Overall, these findings demonstrated that it is feasible to depict the descending and ascending pathways of the spinal cord in live animals using pathway-specific DTT, and demonstrate the usefulness of DTT as an imaging method to assess specific pathways in spinal cord injuries.

Discussion

Because we hope to clinically apply this procedure to human SCI patients in the future, common marmosets were selected for this study. As primates, they are closely related to humans in terms of neurofunctional anatomy of the spinal cord. For example, the CST fibers localize mainly in the dorsal funiculus in rodents, whereas in primates they are mainly located in the lateral funiculus (Qiu et al., 1991; Terashima et al., 1994; Lacroix et al., 2004; Lemon et al., 2004; Iwanami et al., 2005a). From a practical standpoint, common marmosets are easy to handle, breed effectively, and are small enough to fit into the narrow MRI coil.

In our past studies of SCI in common marmosets, we have used contusion injury models because, compared with other SCI methods, contusion injuries more closely resemble the pathological conditions found in human SCI patients (Iwanami et al., 2005a,b). In this study, however, we chose a hemisection model because the disruption and regeneration of axons after a hemisection injury is easier to evaluate than a contusion injury (Levi et al., 2002; Tuszynski et al., 2002). Because the main objective of this study was to evaluate the usefulness of DTT in assessing axonal
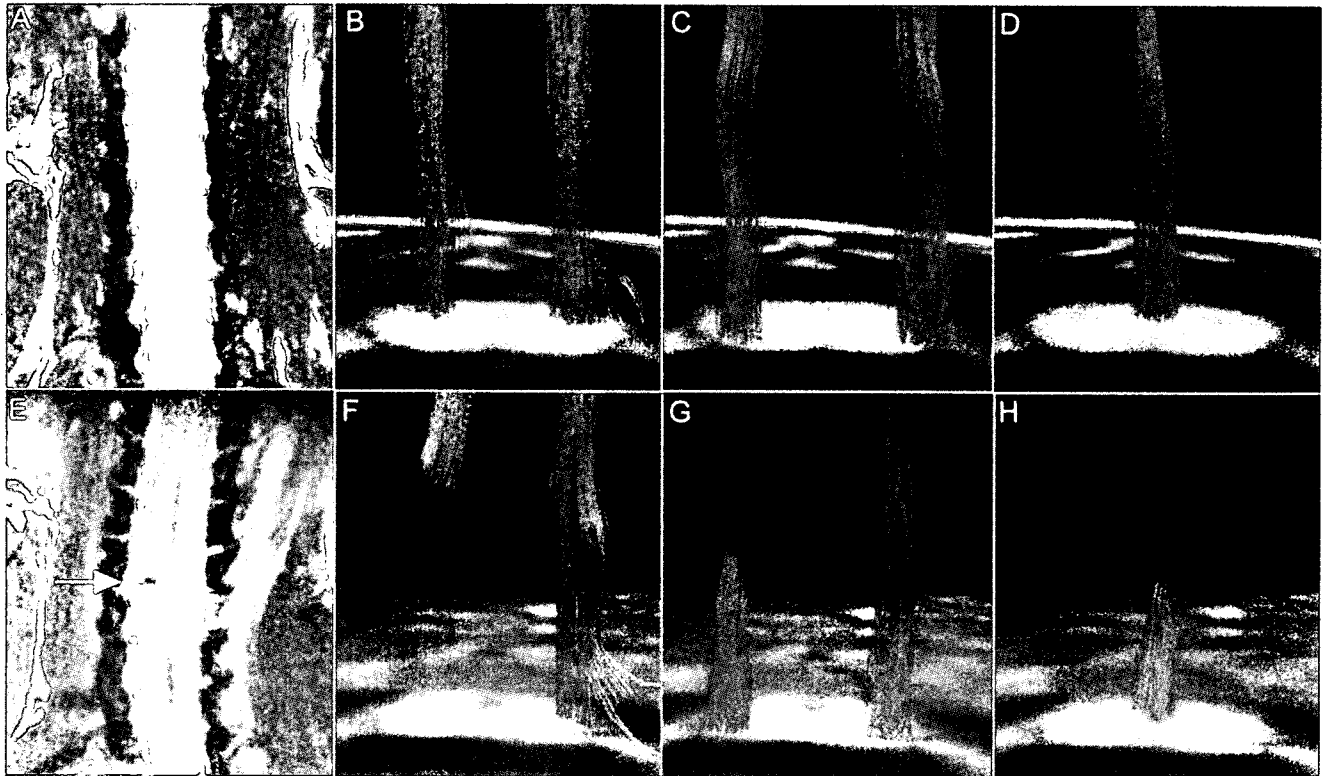
Figure 5. *A–H, In vivo* pathway-specific DTT of intact and injured spinal cords in live common marmosets. MRI and tract-specific DTT of the intact spinal cord (*A–D*) and hemisected spinal cord 2 weeks after injury (*E–H*). DTTs of the CST (*B, F*), spinothalamic tract (*C, G*), and dorsal column-medial lemniscus pathway (*D, H*) were conducted in both groups, revealing tract disruption at the hemisection site (C5/6 level) in all pathways. Although there are some limitations, pathway-specific *in vivo* DTT conducted in live animals yielded results similar to those observed in postmortem animals, especially in respect to major tract morphology.

conditions in SCI and to confirm the accuracy of DTT by comparing DTT images with histological findings, an injury with less complexity and ambiguousness was desired. With the convincing images obtained in this study, it would be interesting to examine contusion injury models in the future.

With the ability to visualize axonal projections in three-dimensions, DTT has tremendous potential as a tool to diagnose and evaluate CNS disease and trauma. In fact, DTT is already being clinically applied to visualize cerebral long tracts in cerebral surgery (Kamada et al., 2005b; Okada et al., 2006). Although there have been several preliminary studies of spinal cord DTI and DTT, they have not fully explored the potential of DTI technology. One reason DTI of the spinal cord has been less studied compared with the brain is the technical difficulty involved in conducting imaging of the spinal cord. DTI of the spinal cord requires high spatial resolution, is easily affected by magnetic susceptibility, and is obscured by *in vivo* bulk motion brought about by the beating of the heart, respiration, and the flow of CSF (Basser and Jones, 2002; Maier and Mamata, 2005; Kharbanda et al., 2006). In the present study, a 7.0 tesla MRI was used to obtain images with high resolution and a spin echo protocol was used to minimize magnetic susceptibility. To eliminate the effect of *in vivo* bulk motion, we first conducted our study using postmortem animals. Because a previous study demonstrated a degradation of diffusion anisotropy in the postmortem spinal cord (Matsuzawa et al., 1995; Madi et al., 2005), we performed all imaging immediately after animals were killed. By using postmortem animals it was possible to conduct scans of long duration (an average scan time of 10 h), resulting in images with high spatial resolution.

In our study using live animals, all animals were maintained under general anesthesia and cardiac-gated imaging was incorporated to minimize the effects of bulk motion. Under general anesthesia, marmosets were immobilized on an acrylic bed with a specially designed head positioner. Because the total scan duration was limited by anesthetic considerations, scan time (average 1.5 h) and, therefore, scan area and spatial resolution were limited compared with postmortem animal studies. However, it is of enormous importance that DTT of a live animal was able to visualize intact neural pathways and also the disrupted pathways in an injured animal, because this is the only method currently available or in development that can reveal *in vivo* axonal pathways.

In this study, we focused mainly on the CST to conduct pathway-specific DTT because it is the most important pathway in terms of motor function and often becomes the subject of scrutiny in studies of spinal cord injury treatment protocols. CST-specific DTT accurately depicted the course of the CST from the medulla to the cervical spinal cord and succeeded in imaging the "pyramidal decussation," which has been considered difficult to visualize. Furthermore, CST-specific DTT of the hemisected animal revealed the disruption of the CST at the site of injury. By using the dTV DTT software (Kunimatsu et al., 2003; Masutani et al., 2003), it is also possible to set the ROI at any point of interest and to perform voxel unit fiber tracking from that position within the threshold limit set for diffusion anisotropy. This allowed us to conduct DTT of the afferent pathways in both intact and injured spinal cords, illustrating the enormous value of this method. This capability to visualize specific projections can be applied to various studies of the spinal cord. For example, an

interesting study would be a study of ascending projections and its involvement in allodynia, using functional MRI to assess sensory dysfunction (Hofstetter et al., 2005; Lilja et al., 2006).

DTT is a new technique that traces white matter fiber trajectories by tracking the direction of faster diffusion, which is assumed to correspond to the longitudinal axis of the tract. However it is important to keep in mind that the tracking is conducted in units called voxels, which, in this study, is 0.215 mm in size, considerably larger than any one individual axonal tract. Therefore, what is actually being tracked is a group of axonal fibers with perhaps some tissue other than the intended fibers at times included in the same voxel (Mori and van Zijl, 2002; Mori and Zhang, 2006). When tissues other than the targeted axonal tract are present within the same voxel, their diffusion anisotropy interferes destructively in a phenomenon referred to as partial volume effect (Alexander et al., 2001). For example, if multiple axonal fiber tracts with different trajectories cross within the same voxel, their diffusion anisotropy becomes merged and may become more isotropic, losing directional information. The tracking procedure is often terminated because the path comes to a voxel that has lost directional orientation (anisotropy) as a result of this partial volume effect (Fig. 3A–E). Partial volume effect can also result in a misleading redirection of anisotropy, leading to incorrect fiber tracking. It is also important to understand that the number of tracts traced by DTT does not necessarily reflect the actual volume of white matter fiber trajectories (Fig. 3A–E).

With the convincing images obtained in this study, the possibilities and the limitations of spinal cord DTT need to be further explored. For example, the next step would be DTT of contusion SCI models. Another significant point that needs to be studied, is whether DTT has the sensitivity to detect regenerating axons. If confirmed, DTT would allow tracing studies at multiple time points in the same animal/patient, becoming an indispensable tool to monitor and evaluate the effectiveness of any treatment protocol for spinal cord injury. Whatever the results reveal, DTT of the spinal cord is a powerful tool with tremendous potential if its properties and limitations are fully understood and correctly applied.

References

Alexander AL, Hasan KM, Lazar M, Tsuruda JS, Parker DL (2001) Analysis of partial volume effects in diffusion-tensor MRI. Magn Reson Med 45:770–780.

Basser PJ, Jones DK (2002) Diffusion-tensor MRI: theory, experimental design and data analysis—a technical review. NMR Biomed 15:456–467.

Basser PJ, Pierpaoli C (1996) Microstructural and physiological features of tissues elucidated by quantitative-diffusion-tensor MRI. J Magn Reson B 111:209–219.

Basser PJ, Mattiello J, LeBihan D (1994) MR diffusion tensor spectroscopy and imaging. Biophys J 66:259–267.

Beaulieu C (2002) The basis of anisotropic water diffusion in the nervous system—a technical review. NMR Biomed 15:435–455.

Carpenter MB, Sutin J (1983) Human neuroanatomy, Ed 8, pp 282–289. Baltimore: Lippincott, Williams and Wilkins.

Conturo TE, Lori NF, Cull TS, Akbudak E, Snyder AZ, Shimony JS, McKinstry RC, Burton H, Raichle ME (1999) Tracking neuronal fiber pathways in the living human brain. Proc Natl Acad Sci USA 96:10422–10427.

Ducreux D, Lepeintre JF, Fillard P, Loureiro C, Tadie M, Lasjaunias P (2006) MR diffusion tensor imaging and fiber tracking in 5 spinal cord astrocytomas. AJNR Am J Neuroradiol 27:214–216.

Facon D, Ozanne A, Fillard P, Lepeintre JF, Tournoux-Facon C, Ducreux D (2005) MR diffusion tensor imaging and fiber tracking in spinal cord compression. AJNR Am J Neuroradiol 26:1587–1594.

Hofstetter CP, Holmstrom NA, Lilja JA, Schweinhardt P, Hao J, Spenger C, Wiesenfeld-Hallin Z, Kurpad SN, Frisen J, Olson L (2005) Allodynia limits the usefulness of intraspinal neural stem cell grafts; directed differentiation improves outcome. Nat Neurosci 8:346–353.

Holder CA, Muthupillai R, Mukundan Jr S, Eastwood JD, Hudgins PA (2000) Diffusion-weighted MR imaging of the normal human spinal cord in vivo. AJNR Am J Neuroradiol 21:1799–1806.

Ito R, Mori S, Melhem ER (2002) Diffusion tensor brain imaging and tractography. Neuroimaging Clin N Am 12:1–19.

Iwanami A, Yamane J, Katoh H, Nakamura M, Momoshima S, Ishii H, Tanioka Y, Tamaoki N, Nomura T, Toyama Y, Okano H (2005a) Establishment of graded spinal cord injury model in a nonhuman primate: the common marmoset. J Neurosci Res 80:172–181.

Iwanami A, Kaneko S, Nakamura M, Kanemura Y, Mori H, Kobayashi S, Yamasaki M, Momoshima S, Ishii H, Ando K, Tanioka Y, Tamaoki N, Nomura T, Toyama Y, Okano H (2005b) Transplantation of human neural stem cells for spinal cord injury in primates. J Neurosci Res 80:182–190.

Kamada K, Todo T, Morita A, Masutani Y, Aoki S, Ino K, Kawai K, Kirino T (2005a) Functional monitoring for visual pathway using real-time visual evoked potentials and optic-radiation tractography. Neurosurgery 57 [Suppl]:121–127.

Kamada K, Todo T, Masutani Y, Aoki S, Ino K, Takano T, Kirino T, Kawahara N, Morita A (2005b) Combined use of tractography-integrated functional neuronavigation and direct fiber stimulation. J Neurosurg 102:664–672.

Kaneko S, Iwanami A, Nakamura M, Kishino A, Kikuchi K, Shibata S, Okano HJ, Ikegami T, Moriya A, Konishi O, Nakayama C, Kumagai K, Kimura T, Sato Y, Goshima Y, Taniguchi M, Ito M, He Z, Toyama Y, Okano H (2007) A selective Sema3A inhibitor enhances regenerative responses and functional recovery of the injured spinal cord. Nat Med 12:1380–1389.

Kharbanda HS, Alsop DC, Anderson AW, Filardo G, Hackney DB (2006) Effects of cord motion on diffusion imaging of the spinal cord. Magn Reson Med 56:334–339.

Kulkarni MV, Williams JC, Yeakley JW, Andrews JL, McArdle CB, Narayana PA, Howell RR, Jonas AJ (1987) Magnetic resonance imaging in the diagnosis of the cranio-cervical manifestations of the mucopolysaccharidoses. Magn Reson Imaging 5:317–323.

Kunimatsu A, Aoki S, Masutani Y, Abe O, Mori H, Ohtomo K (2003) Three-dimensional white matter tractography by diffusion tensor imaging in ischaemic stroke involving the corticospinal tract. Neuroradiology 45:532–535.

Lacroix S, Havton LA, McKay H, Yang H, Brant A, Roberts J, Tuszynski MH (2004) Bilateral corticospinal projections arise from each motor cortex in the macaque monkey: a quantitative study. J Comp Neurol 473:147–161.

Le Bihan D, Breton E, Lallemand D, Grenier P, Cabanis E, Laval-Jeantet M (1986) MR imaging of intravoxel incoherent motions: application to diffusion and perfusion in neurologic disorders. Radiology 161:401–407.

Lee JS, Han MK, Kim SH, Kwon OK, Kim JH (2005) Fiber tracking by diffusion tensor imaging in corticospinal tract stroke: topographical correlation with clinical symptoms. NeuroImage 26:771–776.

Lemon RN, Kirkwood PA, Maier MA, Nakajima K, Nathan P (2004) Direct and indirect pathways for corticospinal control of upper limb motoneurons in the primate. Prog Brain Res 143:263–279.

Levi AD, Dancausse H, Li X, Duncan S, Horkey L, Oliviera M (2002) Peripheral nerve grafts promoting central nervous system regeneration after spinal cord injury in the primate. J Neurosurg 96:197–205.

Lilja J, Endo T, Hofstetter C, Westman E, Young J, Olson L, Spenger C (2006) Blood oxygenation level-dependent visualization of synaptic relay stations of sensory pathways along the neuroaxis in response to graded sensory stimulation of a limb. J Neurosci 26:6330–6336.

Madi S, Hasan KM, Narayana PA (2005) Diffusion tensor imaging of in vivo and excised rat spinal cord at 7 T with an icosahedral encoding scheme. Magn Reson Med 53:118–125.

Maier SE, Mamata H (2005) Diffusion tensor imaging of the spinal cord. Ann NY Acad Sci 1064:50–60.

Masutani Y, Aoki S, Abe O, Hayashi N, Otomo K (2003) MR diffusion tensor imaging: recent advance and new techniques for diffusion tensor visualization. Eur J Radiol 46:53–66.

Matsuzawa H, Kwee IL, Nakada T (1995) Magnetic resonance axonography of the rat spinal cord: postmortem effects. J Neurosurg 83:1023–1028.

Mori H, Masutani Y, Aoki S, Abe O, Hayashi N, Masumoto T, Yamada H, Yoshikawa T, Kunimatsu A, Ohtomo K, Kabasawa H (2003) [Simple visualization of the corticospinal pathway using tractography: one-ROI

and two-ROI methods]. Nippon Igaku Hoshasen Gakkai Zasshi 63:51–53.

Mori S, van Zijl PC (2002) Fiber tracking: principles and strategies—a technical review. NMR Biomed 15:468–480.

Mori S, Zhang J (2006) Principles of diffusion tensor imaging and its applications to basic neuroscience research. Neuron 51:527–539.

Moseley ME, Cohen Y, Kucharczyk J, Mintorovitch J, Asgari HS, Wendland MF, Tsuruda J, Norman D (1990) Diffusion-weighted MR imaging of anisotropic water diffusion in cat central nervous system. Radiology 176:439–445.

Okada T, Mikuni N, Miki Y, Kikuta K, Urayama S, Hanakawa T, Fushimi Y, Yamamoto A, Kanagaki M, Fukuyama H, Hashimoto N, Togashi K (2006) Corticospinal tract localization: integration of diffusion-tensor tractography at 3-T MR imaging with intraoperative white matter stimulation mapping—preliminary results. Radiology 240:849–857.

Olson L (2002) Med: clearing a path for nerve growth. Nature 416:589–590.

Pajevic S, Pierpaoli C (1999) Color schemes to represent the orientation of anisotropic tissues from diffusion tensor data: application to white matter fiber tract mapping in the human brain. Magn Reson Med 42:526–540.

Qiu Y, Wada Y, Otomo E, Tsukagoshi H (1991) Morphometric study of cervical anterior horn cells and pyramidal tracts in medulla oblongata and

the spinal cord in patients with cerebrovascular diseases. J Neurol Sci 102:137–143.

Ralston DD, Ralston III HJ (1985) The terminations of corticospinal tract axons in the macaque monkey. J Comp Neurol 242:325–337.

Stejskal EO, Tanner JE (1965) Spin diffusion measurements: spin echoes in the presence of a time dependent field gradient. J Chem Phys 42:288–292.

Terashima T, Ochiishi T, Yamauchi T (1994) Immunohistochemical detection of calcium/calmodulin-dependent protein kinase II in the spinal cord of the rat and monkey with special reference to the corticospinal tract. J Comp Neurol 340:469–479.

Tsuchiya K, Fujikawa A, Suzuki Y (2005) Diffusion tractography of the cervical spinal cord by using parallel imaging. AJNR Am J Neuroradiol 26:398–400.

Tuszynski MH, Grill R, Jones LL, McKay HM, Blesch A (2002) Spontaneous and augmented growth of axons in the primate spinal cord: effects of local injury and nerve growth factor-secreting cell grafts. J Comp Neurol 449:88–101.

Yamashita Y, Takahashi M, Matsuno Y, Sakamoto Y, Oguni T, Sakae T, Yoshizumi K, Kim EE (1990) Chronic injuries of the spinal cord: assessment with MR imaging. Radiology 175:849–854.

Hepatocyte growth factor (HGF) attenuates gliosis and motoneuronal degeneration in the brainstem motor nuclei of a transgenic mouse model of ALS

Keiichi Kadoyama, Hiroshi Funakoshi, Wakana Ohya, Toshikazu Nakamura *

*Division of Molecular Regenerative Medicine, Department of Biochemistry and Molecular Biology,
Osaka University Graduate School of Medicine, Osaka 565-0871, Japan*

Abstract

Amyotrophic lateral sclerosis (ALS) is a fatal neurodegenerative disease characterized by progressive loss of brainstem and spinal motoneurons. Although prevention of motoneuronal degeneration has been postulated as the primary target for a cure, accumulating evidence suggests that microglial accumulation contributes to disease progression. This study was designed to assess the ability of HGF to modulate microglial accumulation and motoneuronal degeneration in brainstem motor nuclei, using double transgenic mice overexpressing mutated $SOD1^{G93A}$ and HGF (G93A/HGF). Histological and immunohistochemical analyses of the tissues of G93A/HGF mice revealed a marked decrease in the number of microglia and reactive astrocytes and an attenuation of the loss of motoneurons in facial and hypoglossal nuclei compared with G93A mice. HGF overexpression attenuated monocyte chemoattractant protein-1 (MCP-1) induction, predominantly in astrocytes; suppressed activation of caspase-1, -3 and -9; and, increased X chromosome-linked inhibition of apoptosis protein (XIAP) in the motoneurons of G93A mice. The implication is that HGF reduces microglial accumulation by suppressing MCP-1 induction and prevents motoneuronal death through inhibition of pro-apoptotic protein activation. These findings suggest that, in addition to direct neurotrophic activity on motoneurons, HGF-suppression of gliosis may retard disease progression, making HGF a potential therapeutic agent for the treatment of ALS patients.
© 2007 Elsevier Ireland Ltd and the Japan Neuroscience Society. All rights reserved.

Keywords: Caspases; X chromosome-linked inhibitor of apoptosis protein (XIAP); Microglia; Monocyte chemoattractant protein-1 (MCP-1); c-Met

1. Introduction

Amyotrophic lateral sclerosis (ALS) is a fatal neurodegenerative disease characterized by progressive degeneration of motoneurons and their axons in the brainstem and spinal cord, leading to spasticity, hyperreflexia, generalized weakness of the limbs, muscle atrophy, and paralysis (Cleveland and Rothstein, 2001). Most cases (90%) are classified as sporadic ALS (SALS), as they are not associated with a documented family history. The remaining 10% are inherited and referred to as familial ALS (FALS). Gene mutations in copper/zinc superoxide dismutase 1 (SOD1) are responsible for 15–20% of FALS. In addition, mutations in the ALS2/alsin, senataxin (SETX), synaptobrevin/vesicle-associated membrane protein-

associated protein B (VAPB) and dynactin genes recently have been associated with ALS (Pasinelli and Brown, 2006). Regardless of the type of gene mutations or whether the disease is familial or sporadic, motoneuronal degeneration is thought to constitute a common and primary event in ALS (Cleveland and Rothstein, 2001). Therefore, most efforts have been directed toward finding molecules that act directly on motoneurons in an attempt to reduce their degeneration, regardless of the effects of gliosis on surrounding motoneurons. However, treatment with minocycline, an antibiotic that inhibits microglial activation (Yrjanheikki et al., 1999; Van Den Bosch et al., 2002; Zhu et al., 2002), was found to slow disease progression in a transgenic mouse model of ALS that overexpresses mutated human $SOD1^{G93A}$ (G93A) (Kriz et al., 2002). Boillee et al. (2006) recently used the Cre-lox system to show that diminishing expression of mutated $SOD1^{G37R}$ in the microglia of a transgenic mouse model of ALS prolongs disease duration and survival. These lines of evidence demonstrate that

_____
* Corresponding author. Tel.: +81 6 6879 3783; fax: +81 6 6879 3789.
E-mail address: nakamura@onbich.med.osaka-u.ac.jp (T. Nakamura).

microglia might contribute to disease progression that is caused by mutant SOD1 toxicity in a transgenic mouse model of ALS and raises the possibility that reducing the number of activated microglia could be incorporated as another strategy for ALS therapy.

Hepatocyte growth factor (HGF) was initially identified and molecularly cloned as a potent mitogen for mature hepatocytes (Nakamura et al., 1984, 1989). Subsequent studies revealed that HGF exerts multiple biological effects, including mitogenic, motogenic, morphogenic, and anti-apoptotic activities in a wide variety of cells, including neurons, by binding to the c-Met receptor tyrosine kinase (c-Met) (Funakoshi and Nakamura, 2003). HGF is one of the most potent *in vitro* and *in vivo* survival-promoting factors for neurons. For example, neurotrophic effects of HGF have been demonstrated in cultured hippocampal neurons (Honda et al., 1995) and in cultured embryonic spinal motoneurons (Ebens et al., 1996; Yamamoto et al., 1997; Novak et al., 2000), and its anti-apoptotic activity in motoneurons is comparable to that of glial cell line-derived neurotrophic factor (GDNF) (Ebens et al., 1996). Indeed, reflecting the *in vitro* neurotrophic activity of HGF on motoneurons and the expression of c-Met in motoneurons of G93A mice, the transgenic overexpression of rat HGF in the nervous system attenuates spinal motoneuronal death and axonal degeneration, delays onset of the disease and prolongs the lifespan of G93A mice (Sun et al., 2002). However, many studies have suggested that some neurotrophic factors show survival-promoting effects only on certain subtypes of motoneurons in the spinal cord and brainstem (Sakamoto et al., 2003; Guillot et al., 2004). Therefore, the effects of HGF on the degeneration of ALS brainstem motoneurons in G93A mice remain unclear. Furthermore, the role of HGF on microglial accumulation, another research target in the search for an ALS cure, is poorly understood. In the present study, the effects of HGF on microglial accumulation and motoneuronal degeneration in brainstem (facial and hypoglossal) motor nuclei of G93A mice were examined using double transgenic mice overexpressing mutated human $SOD1^{G93A}$ and HGF. The molecular mechanisms by which HGF functions in suppressing microglial accumulation and attenuating motoneuronal degeneration in G93A mice were also examined.

2. Materials and methods

2.1. Animals

Neuron-specific enolase promoter-driven HGF transgenic (HGF-Tg) mice were generated as previously described (Sun et al., 2002). Transgenic mice overexpressing mutated (glycine to alanine in position 93) human SOD1 (G93A) [B6SJL-TgN (SOD1-G93A)^{dl}Gur1] (Gurney et al., 1994) were purchased from the Jackson Laboratory (Bar Harbor, ME). This mouse strain has a low copy number of $SOD1^{G93A}$ and shows a delayed onset of ALS, slower disease progression, and a longer lifespan compared with mice carrying a high copy number of the transgene (G1H). This strain resembles the slow progressing phenotype of patients with ALS and is useful for the accurate evaluation of the molecular mechanisms involved in the action of HGF during disease progression. HGF-Tg mice were crossed with G93A transgenic mice to generate G93A/HGF-double transgenic animals. The HGF and G93A transgenic heterozygous mice were maintained by mating transgenic males with C57/BL6 females.

Mouse genotypes were determined by polymerase chain reaction (PCR) and Southern blot analysis as previously reported (Gurney et al., 1994; Sun et al., 2002). Non-transgenic littermates served as controls. Experimental protocols were approved by the Animal Experimentation Ethics Committee of Osaka University Graduate School of Medicine. All efforts were made to minimize animal discomfort and the number of animals used.

2.2. Tissue preparation

Wild-type (WT), HGF-Tg, G93A, and G93A/HGF mice at 6 and 8 months of age were sacrificed with an overdose injection of pentobarbital sodium salt. Tissues were fixed by treating them in increasing concentrations of ethanol. After dehydration, the tissues were treated with xylene and embedded in paraffin. Serial tissue sections were cut on a microtome to a thickness of 7 μm, deparaffinized, and used for either Nissl staining or for immunohistochemistry.

2.3. Motoneuron survival

The neuroprotective effect of HGF on facial and hypoglossal motoneurons was evaluated by counting the number of motoneurons (i.e., motoneuronal survival). The number of motoneurons in the facial and hypoglossal nuclei of WT, HGF-Tg, G93A, and G93A/HGF mice were counted in every fifth section of 16 Nissl-stained 7-μm-thick paraffin sections ($n = 4$). Densely stained motoneurons with a clear nucleolus and in a defined area of facial and hypoglossal nuclei were counted using Win ROOF analysis software (Mitani Corp., Fukui, Japan) as previously described (Sun et al., 2002).

2.4. HGF ELISA

HGF protein levels in the brainstem of WT and HGF-Tg mice were measured by ELISA using an anti-rat HGF polyclonal antibody (Tokushu Meneki, Tokyo, Japan) as previously described (Sun et al., 2002).

2.5. Immunohistochemistry

The sections were stained with the following antibodies: (i) c-Met polyclonal antibody (1:50; Santa Cruz Biotech, Santa Cruz, CA); (ii) tubulinβIII monoclonal antibody (1:500; Berkeley Antibody Co. Inc., Richmond, CA); (iii) caspase-1 (p10) polyclonal antibody (1:100; Santa Cruz Biotech); (iv) active caspase-3 polyclonal antibody (1:200; Promega, Madison, WI) (v) cleaved caspase-9 polyclonal antibody (1:50; Cell Signaling Technology, Beverly, MA); (vi) X chromosome-linked inhibitor of apoptosis protein (XIAP) monoclonal antibody (1:50; BD Pharmingen, San Diego, CA); (vii) glial fibrillary acidic protein (GFAP) monoclonal antibody (1:500; Chemicon International, Temecula, CA); (viii) Iba1 polyclonal antibody (1:2000; Wako Pure Chemical, Osaka, Japan); and (ix) monocyte chemoattractant protein (MCP)-1 polyclonal antibody (1:100; Abcam, Cambridge, UK). These antibodies were applied to the sections for 1 h at room temperature (RT) or overnight at 4 °C after blocking with phosphate-buffered saline (PBS) containing 5% goat serum and 0.1% Triton X-100 at RT for 1 h. After washing the sections with PBS, immunoreactivity (IR) was visualized by incubating them for 20 min at RT with secondary antibodies conjugated with Alexa Fluor 488 (green) or Alexa Fluor 546 (red) diluted 1:500 (Invitrogen, Carlsbad, CA). When double-immunostaining for XIAP and tubulinβIII was performed, antibodies against XIAP and tubulinβIII were labeled with Alexa Fluor 546 and 488, respectively, using a Zenon labeling kit according to the manufacturer's instructions (Invitrogen). These fluorescence-immunostained sections were observed under a LSM 5 PASCAL confocal microscope (Carl Zeiss, Germany). The staining specificity of the antibodies was also assessed by the absence with first antibody or by preincubation with an excess amount of immunized peptide. The intensities of immunoreactivity against GFAP, Iba-1, MCP-1, active caspase-1, -3, -9 and XIAP were determined as previously described (Sun et al., 2002).

2.6. Statistical analysis

Results were expressed as the mean ± S.E. Statistically significant differences among the four groups of mice were assessed by ANOVA, followed by

Scheffe's post hoc test. Statistical significance was defined as $P < 0.05$ or $P < 0.01$.

3. Results

3.1. c-Met is expressed in facial and hypoglossal motoneurons in a transgenic mouse model of ALS

The effect of HGF on gliosis and motoneuronal degeneration was investigated using a mouse model of ALS (G93A) in which mutated human SOD1^{G93A} is overexpressed (Gurney et al., 1994). Expression of the c-Met/HGF receptor (c-Met) was examined in the facial and hypoglossal nuclei of wild-type (WT) and G93A mice. Immunofluorescence analysis with antibodies against c-Met and tubulinβIII (a neuronal marker) showed that c-Met immunoreactivity (IR) was detectable in the facial and hypoglossal nuclei, and that it was localized in the large-size neurons of WT and G93A mice at both 6 (data not shown) and 8 months (Fig. 1a) of age. These results demonstrate that c-Met is present in facial and hypoglossal motoneurons of WT and G93A mice at the ages that correspond to the middle and end stages of the disease.

3.2. Introduction of HGF into the brainstem of transgenic mice overexpressing HGF (HGF-Tg)

The role of HGF was examined using transgenic mice overexpressing rat HGF (HGF-Tg) (Sun et al., 2002). In HGF-Tg mice, exogenous rat HGF mRNA is located specifically in the brain and spinal cord, as evidenced by an RNase protection assay (Sun et al., 2002). An HGF ELISA, which specifically recognizes rodent HGF, revealed that the levels of HGF in the brainstem of HGF-Tg mice were 2-fold higher than in WT mice (Fig. 1b) with no effect on serum HGF levels (data not shown), demonstrating the successful introduction of HGF into the brainstem of HGF-Tg mice.

3.3. Neuroprotective effect of HGF on facial and hypoglossal motoneurons in G93A mice

The effect of HGF on facial and hypoglossal nuclei against ALS was evaluated by generating double transgenic mice (G93A × HGF-Tg) that overexpressed a mutated form of human SOD1^{G93A} and rat HGF (G93A/HGF). This mating resulted in the generation of four groups of mice: (1) WT, (2) HGF-Tg, (3) G93A and (4) G93A/HGF. Nissl staining showed that the facial motoneurons of G93A mice at 8 months of age were atrophic and were present in lower numbers compared with WT and HGF-Tg mice (Fig. 2a), i.e., 55% of WT (Fig. 2b). In contrast, the facial motoneurons of G93A/HGF mice exhibited a healthier morphology (i.e., less atrophic) than those of G93A mice (Fig. 2a). The mean number of facial motoneurons in G93A/HGF mice was significantly larger than that of the G93A mice, and was almost the same as that of WT mice (Fig. 2b).

The hypoglossal motoneurons of G93A mice also were atrophic, and reduced in number compared with WT and HGF-Tg mice (Fig. 2c), with a decrease in mean number to 57% of WT mice (Fig. 2d). Similar to the facial motoneurons of G93A/HGF mice, the hypoglossal motoneurons of G93A/HGF mice also exhibited a healthier morphology than did those of G93A mice (Fig. 2c). The mean number of hypoglossal motoneurons of G93A/HGF mice was significantly larger than that found in G93A mice (Fig. 2d). These results demonstrate that HGF exerts a neuroprotective effect on brainstem motoneurons against ALS-associated neurotoxicity.

3.4. HGF suppresses gliosis in facial and hypoglossal nuclei of G93A mice

The effect of HGF on gliosis in facial and hypoglossal nuclei of G93A mice was examined using antibodies against Iba1
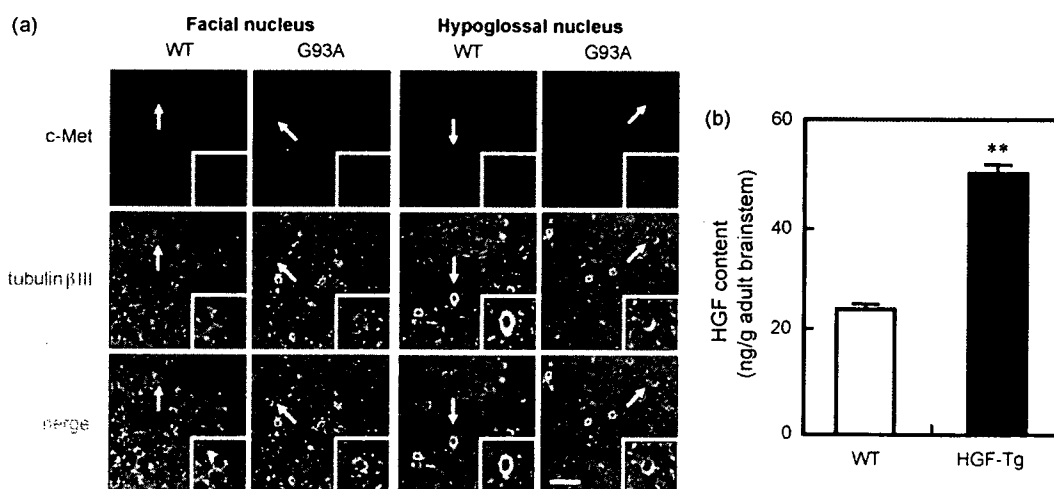

Fig. 1. Expression of c-Met and HGF in the brainstem. (a) Double-immunofluorescence analysis for c-Met (red) and tubulinβIII (green; a marker for neurons) in the facial and hypoglossal nuclei of WT and G93A mice at 8 months of age. A high-magnification view of the area indicated by the arrow is also boxed in each photo. c-Met immunoreactivity was detectable in large-sized neurons of the facial and hypoglossal nuclei. Scale bar = 50 μm. (b) Protein levels of HGF in the brainstems of 6-month-old wild-type (WT) and HGF transgenic (HGF-Tg) mice were analyzed by ELISA ($n = 6$ in each group). Data represent the mean ± S.E. **$P < 0.01$ compared with WT mice.